Numerical and Experimental Investigation of the Tip Vortex Flow Induced by an Elliptical Foil

Moustafa Abdel-Maksoud, Ahmed Sahab, Keqi Wang, Mario Felli, Steven Ceccio, Emmanuel Guilmineau, Michel Visonneau, Jan Geese, Julian Kimmerl, Luc Bordier, et al.

35th Symposium on Naval Hydrodynamics
Nantes, France, 7 July - 12 July 2024

Numerical and Experimental Investigation of the Tip Vortex Flow Induced by an Elliptical Foil

Moustafa Abdel-Maksoud[1,*], Ahmed Sahab[1], Keqi Wang[1], Mario Felli[2], Steven Ceccio[3], Emmanuel Guilmineau[4], Michel Visonneau[4], Jan Geese[5], Julian Kimmerl[5], Luc Bordier[6], Jean-Charles Poirier[6], Johan Bosschers[7], Bente Meijerink[7], Rickard Bensow[8]

[1]Hamburg University of Technology (TUHH), Germany
[2]National Research Council (CNR), Italy
[3]University of Michigan, USA
[4]LHEEA Lab, ECN/CNRS, Nantes, France
[5]SCHOTTEL GmbH, Germany
[6]NAVAL GROUP, SIREHNA, France
[7]Maritime Research Institute Netherlands (MARIN)
[8]Chalmers University of Technology, Sweden
[*]Corresponding author, E-mail: m.abdel-maksoud@tuhh.de

Topic Category: Hydrodynamics of Propulsors and Lifting surfaces, Cavitation and Multi-phase Flows, Fundamentals of Fluid Dynamics in the Naval Context

ABSTRACT

This collaborative paper within the AVT-320 joint research activity compares Computational Fluid Dynamics (CFD) results from diverse methods across research partners, validated against Experimental Fluid Dynamics (EFD) investigations in two test facilities. Focusing on non-cavitating tip vortex flows using an elliptical foil as a test case, the study reveals flow fluctuations and highlights the synergy between research institutions and advanced measurement technologies. The evaluation of CFD methods, including hybrid RANS/LES-numerical approaches, provides insights into turbulence modeling for tip vortex flows. Strong interactions between the tip region and trailing edge flow are observed, contributing to refining our understanding of these complex fluid dynamics. The study includes a comprehensive analysis of the tip vortex behavior of the the elliptical foil NACA 66_2-145, which has been investigated over the past three decades. The collected data encompasses the distribution of 19 flow variables on 17 cross sections, with a detailed analysis and comparison performed on four planes. Experimental results elucidate the effects of wandering correction on variable distribution. Two approaches to model turbulence are employed in CFD computations: scale-resolved simulation models to characterise the local flow and the eddy viscosity-based $k-\omega$ SST model. The hybrid turbulence model ensures consistency in velocity and pressure in the core region, serving as a robust reference for cavitation inception.

INTRODUCTION

Turbulent cavitating flows pose substantial challenges in propulsion, maneuvering, and high-speed scenarios. The complexity arises from the inherently intricate physics of high-Reynolds-number multi-phase flows and phase changes, especially in cavitating vortex flows. Accurately predicting these flows remains challenging due to high velocity gradients and strong interactions among various flow regimes, including tip vortex flow, free vortices from the trailing edge, roll-up processes, and interactions with the free stream flow.

Recent advancements in measurement techniques, employing optical systems like Tomographic Particle Image velocimetry (TPIV) or Stereo Particle Image Velocimetry (SPIV), offer high-precision capturing of tip vortex flows. The temporal and spatial resolutions provided by these techniques enable detailed insights into fundamental flow physics, such as the distribution of the Reynolds stress tensor and mean strain rate.

Addressing challenges in high-fidelity numerical simulations, hybrid URANS/LES methods, requires the deployment of massively parallel computing techniques to enable precise predictions of turbulent flows in the vortex tip region. Recognizing the strategic significance of tip vortex flows in aero- and hydrodynamics, the NATO AVT community has initiated a collaborative effort to assess current technologies, develop best practices, and identify specific areas where improvements are urgently needed. This collaborative effort is embedded in the AVT-320 joint research activity, focusing on a comprehensive

comparative analysis of CFD methods across research partners, validated by Experimental Fluid Dynamics (EFD) investigations.

Trailing vortex flow was identified as critical phenomenon in turbulent flows, early in the aerodynamics field with theoretical descriptions ranging from the simple inviscid Rankine vortex model [1] with a solid rotation inside the viscous core and a potential vortex distribution outside, to the Burgers [14] and Lamb-Oseen vortex [22] to the Batchelor vortex model [10], which assumes that axial flow gradients are negligible compared to the radial components. By applying high resolution methods in space and time, experimental and numerical examination of the these theoretical considerations is possible such as for a planar NACA0012 half-foil with a flat tip [6] and rounded tip [7] [9] with a detailed investigation of the trailing vortex in integral mean values and spatial distribution on intersection planes normal to the vortex trajectory. The latter show that the secondary vortex sheet has to be considered when interpreting circumferential averaging of quantities around the vortex core. While the planar hydrofoil trailing vortex is generated by complex mixing of three different prominent source vortices between the trailing and leading edge on both pressure and suction side, the elliptical NACA66$_2$−145 foil investigated experimentally [2] and numerically [4] features a simpler trailing vortex generation with a clear origin at the tip of the foil and as such is an ideal candidate for the study of the internal axial structure of a trailing vortex and its streamwise evolution.

The elliptical foil serves as a test case, providing a platform to refine turbulence modeling approaches and deepen the understanding of complex interactions governing tip vortex flows. The study encompasses experimental investigations at two large test facilities namely the wind tunnel of Hamburg University of Technology (TUHH) and water circulating channel National Research Council (CNR) and numerical simulations with a special focus on turbulent viscosity in the core region. Insights gained contribute to the advancement of turbulence modeling approaches and enhance our understanding of these intricate fluid dynamics.

APPROACH

This section contains a description of the extensive experimental and numerical investigations carried out for the elliptical foil.

Elliptical Foil Geometry

The experimental setup largely corresponds to that of Delft University of Technology [23], with a notable modification in scale to enhance data resolution. A new foil model with a scale factor approximately 6.67 times larger than the Delft model is manufactured. To maintain consistency, the trailing edge was trimmed by 2 mm, preserving the scale factor. Polyurethane (Sikablock® N980) was used to manufacture the foil, that undergoes testing at both TUHH and CNR. The foil has heat distortion temperature (HDT_{foil}) of $80°C$. The foil main features and characteristics are outlined in Table 1.

Table 1: Foil features in experimental investigations.

Designation	Symbol	Unit	Dimension
Span	L	m	1.000
Chord length (root)	c	m	0.836
Wing area	A	m^2	0.651
Density	ρ_{foil}	g cm^{-3}	1.34
Young's Modulus	E_{foil}	MPa	4000
Flexural strength	F_{foil}	MPa	145
Compressive strength	C_{foil}	MPa	120

A steel cylindrical shaft, secured by ISO M8×25 screws, is mounted in the root section of the foil. Figure 1 visually depicts the foil's construction. The fixation shaft is strategically positioned at a lateral offset of 19.9 mm from the nose-to-trailing-edge line towards the suction side. In the streamwise direction, the fixation shaft maintains an offset of 382.36 mm from the leading edge and 454.76 mm from the trailing edge. The fixation shaft is located at the origin of the coordinate system. The coordinate system is oriented such that the x-direction represents the streamwise direction at zero angle of attack. The y-direction follows the right-hand rule, and the z-direction is aligned as the spanwise direction.

Figure 2 and Figure 3 display the elliptical foil within the experimental environments of TUHH and CNR, respectively. In the TUHH facility, the foil was securely mounted on the ground in the wind tunnel with a precise offset gap of 2 mm to the floor. On the other hand, in the CNR facility, the foil was affixed to a movable carriage suspended from the ceiling within the water channel, with no offset applied.

For the numerical simulations, the same set-up as used by Pennings et al. [23] in the studies at Delft University of Technology was applied. The foil's main characteristics are detailed in Table 2. The coordinate system is defined by the mid-chord at the root, aligning with the experimental evaluation's origin. The angle of attack (AoA) is geometrically defined around this origin. Arndt et al. [2] discuss the foil's angle of zero lift, which was set at $\alpha_0 = -2.5°$.

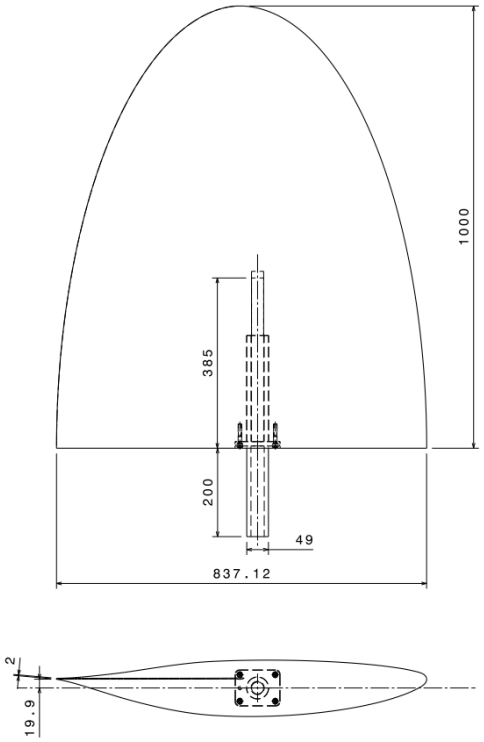

Figure 1: Foil Construction

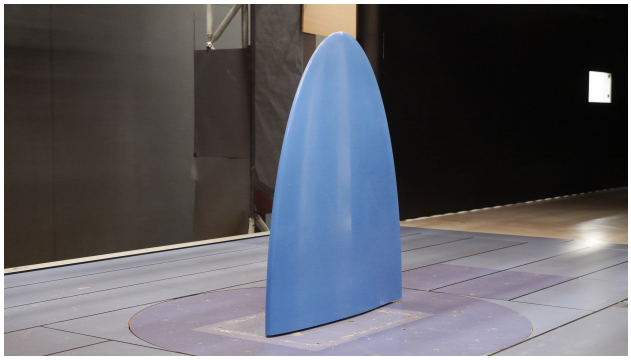

Figure 2: Foil In TUHH Wind Tunnel

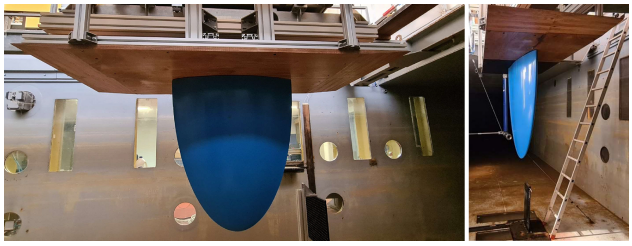

Figure 3: Foil In CNR Circulating Water Channel

Table 2: Foil features used in the numerical investigations.

Designation	Symbol	Unit	Dimension
Span	L	m	0.15
Chord length (root)	c	m	0.1256
Projected area	A	m^2	0.01465

Experimental Approach

TUHH Investigations

The experimental investigations at Hamburg University of Technology (TUHH) took place in the low-speed wind tunnel of the Institute for Fluid Dynamics and Ship Theory (FDS), featuring a $5.5\,\mathrm{m}$ long measuring section with dimensions of $2\,\mathrm{m}$ in height and $3\,\mathrm{m}$ in width. Driven by a $400\,\mathrm{kW}$ blower, the wind tunnel allows velocities between $2.5\,\mathrm{m\,s^{-1}}$ and $45\,\mathrm{m\,s^{-1}}$.

The facility can be operated in two modes, the open circulation (Eiffel mode) and closed loop circulation (Göttingen mode). In Eiffel mode, external fresh air is supplied to prevent smoke accumulation during qualitative visualisation tests, while Göttingen mode preserves seeding particles for quantitative investigations.

The detailed examination involves 15 measurement planes at a flow speed of $16.4\,\mathrm{m\,s^{-1}}$ and two angles of attack: $7°$ and $9°$. The Reynolds number, based on root chord length, is set at 9.1×10^5, ensuring comparable results to previous studies [23]. The experimental setup includes a load cell under the floor for force measurements, and the foil is aligned using the trailing edge offset.

A Tomographic Particle Image Velocimetry System (TPIV), comprising four cameras and a Nd:YLF-laser, captures the vortex structures. The quantitative investigation focuses on the tip vortex, tracking its evolution, wandering behavior, and interaction with flow structures. Seeding particles are generated using a droplet generator in the aft of the test section and are circulated in the whole circulation loop of the wind tunnel, ensuring a homogeneous distribution.

Calibration employs a standard $309 - 15$ calibration target in nine planes, ensuring consistency across measurement stations. The investigation covers 3000 image pairs at each station, capturing high-frequency vortex wandering behavior. The setup allows for precise tracking and analysis of vortical structures in the wake of the elliptical foil.

The uncertainty analysis is conducted following the guidelines of the International Towing Tank Conference (ITTC), [13]. The estimated average

uncertainties of the three velocity components are $w = \pm 0.08\,\mathrm{m\,s^{-1}}$, $v = \pm 0.06\,\mathrm{m\,s^{-1}}$ and $u = \pm 0.33\,\mathrm{m\,s^{-1}}$. The average relative uncertainties of the velocity components to the free stream velocity are $w = \pm 0.80\%$, $v = \pm 0.60\%$ and $u = \pm 3.30\%$.

CNR Investigations

The experiments were conducted at CNR-INM's large free-surface circulating water channel, one of the world's largest facilities of its kind. The test section measures $10\,\mathrm{m}$ in length, $3.6\,\mathrm{m}$ in width and $3\,\mathrm{m}$ in depth with a water depth of $2.25\,\mathrm{m}$ as well as flow speeds up to $5.3\,\mathrm{m\,s^{-1}}$. Notably, the facility can be depressurized down to $3\,\mathrm{kPa}$ for cavitation similitude testing. The water flow is driven by dual 4-bladed axial impellers, each delivering $435\,\mathrm{kW}$. The facility accommodates various operational settings, including a cavitation channel, water flume, and water tunnel.

Extensive measuring systems are integrated, covering dynamometers, torque meters, wave gauges, LDV, PIV, Stereo-PIV, Tomographic PIV, high-speed cameras, and hydroacoustics sensors. Flow measurements are conducted in 19 planes orthogonal to the x-axis to analyze vortex cross-sections, documented in detail (see Table 3 and Figure 4).

Table 3: Investigation planes.

Plane	x/c	Plane	x/c	Plane	x/c
P0	0.000	P11	0.677	P18	1.354
P5	0.019	P12	0.750	P19	1.592
P6	0.199	P13	0.876	P20	2.000
P7	0.279	P14	0.955	P21	2.389
P8	0.358	P15	1.035	P22	3.000
P9	0.500	P16	1.140		
P10	0.579	P17	1.194		

The foil model, mounted on a 6-component balance, is aligned to the streamwise direction and can move throughout the test section. The foil arrangement, with a shifted trailing edge, enables detailed flow measurements for varying distances from the foil tip without relocating the SPIV setup. Deviations in foil alignment are verified and corrected for each position. The S-PIV system captures detailed flow features using two cameras and a pulsed Nd-Yag laser.

Calibration is performed using a calibration plate, and structural analysis of the foil ensures its integrity under experimental conditions. Stress and deformation distributions indicate safe operation within the model material's limits.

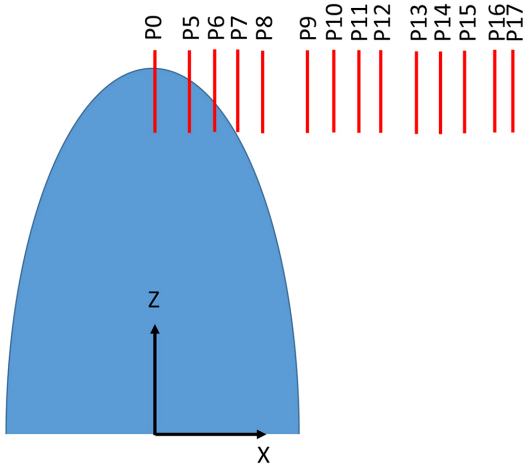

Figure 4: Measurement planes.

Numerical Approach

The main objectives of this numerical study are to improve the understanding of tip vortex flow physics and evaluate the performance of different numerical methods, including URANS and hybrid URANS/LES, in capturing complex flows behind lifting surfaces. Five organizations participated in the numerical study; six contributions were made, with CNRS performing numerical simulations using both RANS and hybrid RANS/LES over different numerical grids. SCHOTTEL and SIREHNA used only the RANS approach, while TUHH used the hybrid RANS/LES approach to simulate the flow characteristics of the tip vortex core. MARIN submitted results of available computations using the hybrid RANS/LES approach performed in cooperation with Delft University of Technology [18]. The study includes a comparative analysis of some key parameters between numerical predictions and experimental data, such as turbulent kinetic energy, vorticity, Reynolds stress tensor, and mean strain rate.

Numerical Variables

In order to allow a reliable comparison with the experiment, the results of the CFD computations are normalized. In the analysis of the numerical results, the additional parameters shown in Table 4 are considered.

Computation Domain and Boundary Conditions

The PIV measurements of Pennings were performed at the free stream velocity $v_\infty = 6.8\,\mathrm{m\,s^{-1}}$ with fluctuations of $\pm 0.5\%$. The corresponding value of the Reynolds number is $R_e = v_\infty c/\nu = 8.54 \times 10^5$, where ν is the kinematic viscosity. The domain cross-section is designed to match the measuring section of the Delft cavitation tunnel, with dimensions [2·c, 2·c]. The extension of the

Table 4: Flow quantities.

Quantities	Symbol
Coordinates	$z' = z/c$, same for x' and y'
Radius	r/r_v, where r_v is the viscous core radius
Inflow velocity	v_∞
Radial circumferential averaged tangential velocity component	$\overline{V_t}$
Radial circumferential averaged radial velocity component	$\overline{V_r}$
Radial circumferential averaged axial velocity component	$\overline{V_a}$
Fluctuations	$u' = u - v_\infty$, same for v' and w'
Lift coefficient	$C_L = F_L/0.5\rho v_\infty^2 A$
Pressure coefficient	$C_p = (p - p_\infty) \,/\, \left(\frac{1}{2}\rho v_\infty^2\right)$
Turbulent Kinetic Energy (TKE)	TKE/v_∞^2
Q-value	$Q \cdot (c/v_\infty)^2$
Circulation	$\Gamma\,(V_{t_{\max}} \cdot r_v)$
Reynolds stress	R

domain from the origin (root center chord) to both the inlet and outlet varies based on the numerical simulations performed for each submission, as detailed in Table 5. The numerical domain and boundary conditions can be found in Figure 5. No slip condition is applied to both the foil and the wall where the foil is mounted, while a slip condition is implemented on the remaining three walls of the measuring section. This is motivated, as in the experiments at TU Delft, the top wall had a slight inclination to compensate for the effect of the growing boundary layers.

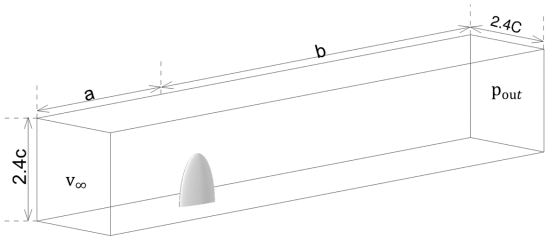

Figure 5: Numerical domain.

Computational Grid

Various approaches of grid generation are employed: unstructured meshes by SCHOTTEL, CNRS, and SIREHNA; structured meshes by MARIN; and hybrid meshes by TUHH. Different mesh resolutions are utilized in various regions, particularly in areas where flow features undergo significant changes, such as within the tip vortex and wake flow. SCHOTTEL employs Adaptive

Table 5: Domain size and boundary conditions.

Institution	a	b	v_∞ [m s^{-1}]	Pout [Pa]
TUHH	6.4·c	25.5·c	6.8	98591
SCHOTTEL	5·c	10·c	6.8	11090
CNRS	4·c	10·c	6.8	0
MARIN	5.5·c	10.5·c	7.15	0
SIREHNA	4·c	10·c	6.8	0

Mesh Refinement (AMR) based on the Q-criterion, while CNRS and SIREHNA uses anisotropic adaptive grid techniques, focusing on flux-component Hessian derived from the second derivatives of velocity fluxes and pressure. MARIN and TUHH, on the other hand, implement a grid with varying levels of refinement, specifically in vortex and wake regions. The mesh information is detailed in Table 6. An overview of the numerical meshes are shown in Figure 6.

Numerical Settings

In all contributions, a low Reynolds number ("low-Re") wall boundary condition is applied, which involves resolving the entire boundary layer using a highly refined mesh. Different approaches are applied in the simulations, focusing on different aspects such as time integration methods, spatial discretization techniques, turbulence modeling and grid generation strategies. This variation in methods demonstrates their respective focuses and specialized optimization techniques for their individual

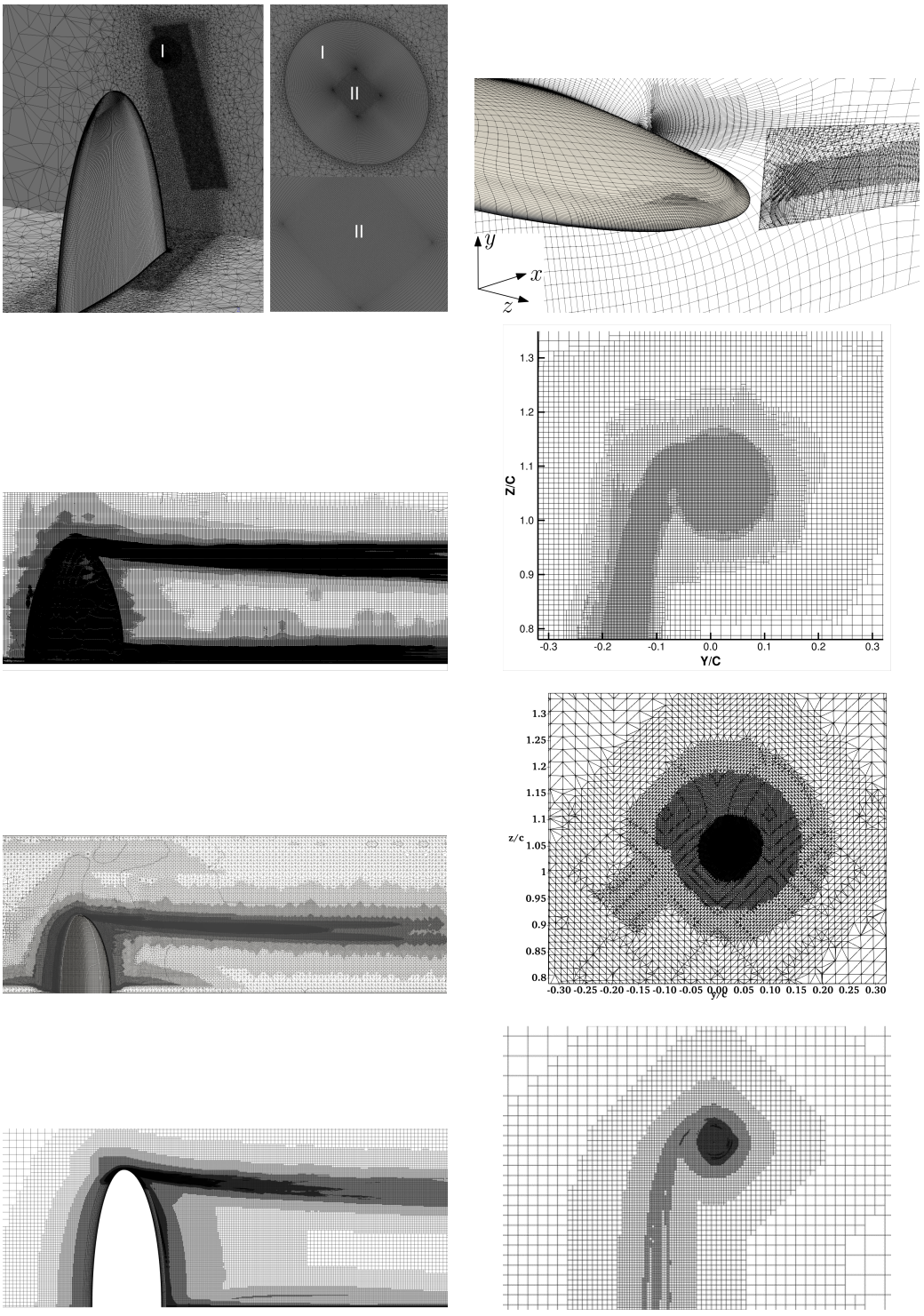

Figure 6: View of the meshes. From top to bottom: TUHH (left) and MARIN (right), CNRS, SCHOTTEL, SIREHNA

numerical simulations as follows:

- **TUHH** applies the solver ANSYS-CFX, which is a commercially available CFD code primarily designed to simulate computational fluid dynamics for turbomachinery applications. A wide range

Table 6: Mesh information in the vortex core region.

Institution	Grid spacing $\times 10^{-4}$ [-]			Total cells [million]
	In-plane		Stream-wise	
	Δy/c	Δz/c	Δx/c	
TUHH	1.11	1.11	9.95	90
SCHOTTEL	7.17	7.17	7.17	105
CNRS	23	23	38	41 & 133
MARIN	17	17	43	7
SIREHNA	4.8	4.8	4.8	44

of turbulence models is implemented. This includes models based on the Reynolds-Averaged Navier-Stokes (RANS) equations, which can be classified as either eddy-viscosity models like SST $k-\omega$ model, or Reynolds stress models such as Explicit Algebraic Reynolds stress model (EARSM), and Baseline (BSL) Reynolds stress model. In addition, different hybrid models are available which can be classified as scale-resolved simulation (SRS) models, such as Scale-Adaptive Simulation (SAS) models, Detached Eddy Simulation (DES) models, Stress-Blended Eddy Simulation (SBES) and Large Eddy Simulation (LES).
In this study, SBES approach was applied. The solver uses central difference (CD) schemes in the LES region but blends with a first-order upwind scheme for stability. A second-order backward Euler scheme was used for time integration.

- **SCHOTTEL** implements a three-stage simulation approach with one time automated Adaptive Mesh Refinement (AMR) to create a coarse and a fine mesh from an inital mesh without refinements. In the OpenFOAM based Engys HELYXcore v3.3.2 the incompressible, isothermal two-phase pressure based solver interPhaseChangeFoam is selected, where a dynamic mesh functionality is only activated during the refinement steps. With the PIMPLE algorithm the unsteady Reynolds-averaged Navier-Stokes (URANS) equations are solved, where the turbulence is modelled with the standard OpenFOAM k-ω SST model under an isotropic assumption. The wall function for turbulent viscosity is according Spalding's Law, the turbulent kinetic energy and the specific dissipation rate are modelled with a viscous sublayer assumption, which is set automatically as the surface mesh achieves $Y^+ < 1$ values. The wetted simulations are realized with a vapor saturation pressure set to practically negative infinity, while the cavitating simulations use the VOF approach with a slow ramping of the saturation pressure. They use first-order time discretization during the AMR phase and second-order on the final mesh.

- **CNRS** employs the solver ISIS-CFD, available as a part of the FINE™/Marine computing suite distributed by Cadence Design Systems, Inc. This solver is an incompressible multiphase URANS solver mainly devoted to marine hydrodynamics. It is based on a fully-unstructured (face-based) finite volume discretization with specific functionalities needed for multiphase flows and industrial applications [26]. The method features several sophisticated turbulence models: apart from the classical two-equation k-ϵ and k-ω models, the anisotropic two-equation Explicit Algebraic Reynolds Stress Model (EARSM), as well as Reynolds Stress Transport Models (SSG/LRR). All models are available with wall-function or low-Reynolds near wall formulations. Hybrid RANS/LES turbulence models based on Detached Eddy Simulation (DES-SST, DDES-SST, IDDES) are also implemented [12]. For this study, only two turbulence models are used: the k-ω SST and the DDES-SST. A centered scheme for diffusion terms and a blended scheme for convective fluxes are applied. The two LCTM-based $\gamma - Re_\theta$, γ) transition models equipped with crossflow criteria have been recently included and validated [28]. Finally, an anisotropic automatic grid refinement procedure has been developed which is controlled by various flow-related criteria [29]. For both turbulence models, Adaptive Mesh Refinement is used [21].

- **MARIN** applies the solver ReFRESCO, which computes multiphase unsteady incompressible viscous flows using the Navier-Stokes equations, together with a wide range of transition, turbulence and cavitation models. The equations are discretized by using the finite volume approach with cell-centered collocated variables, in strong-conservation form. Mass conservation is ensured by using a pressure-correction equation based on the SIMPLE algorithm [15]. Earlier applications of ReFRESCO for vortices and cavitation can be found in [16] [17] [18] [24]. The presented computations were performed applying a second order accurate implicit time integration method and the QUICK scheme for the discretization of convective terms. For turbulence closure, a hybrid RANS-LES approach (Improved Delayed Detached-Eddy Simulation, IDDES) was employed [18].

- **SIREHNA** calculated the flows using the STAR-CCM+ calculation code developed by SIEMENS (version 2022.10). The simulations are carried out in URANS, considering a single, incompressible liquid phase for water. A modified version of Shear-Stress Transport k-ω turbulence model is used for turbulence treatment, the modification consisting of replacing the k production limiter with a Durbin's realizability constraint [8]. The pressure-velocity coupling is solved using the SIMPLE algorithm. The convection of velocity in the momentum equation is discretized using hybrid bounded central differencing scheme. The convection of turbulence terms are treated using second-order upwind scheme. For gradients calculation, the hybrid Gauss and least squares method based on local cell quality with the Venkatakrishnan limiter is used. Implicit second-order upwind Euler time scheme is used for the time advance.

Table 7 gives an overview of the numerical simulations conducted by the participants.

RESULTS

This section includes a comparison of measured and calculated parameters at the P9 test station. P9 was selected for its particular representation of dynamic tip vortex behavior. It provides an optimal compromise between effectively mapping the complexity of the upstream flow while minimising the effects of the downstream meandering eddy flow.

Lift Coefficient

Since the lift coefficient C_L has a strong influence on the tip vortex flow-induced vorticity and the vortical structure behind the trailing edge, a focus is placed on the calculated or measured lift value. As shown in Table 8, the measured values of C_L at TUHH and CNR are significantly lower than the value obtained in the earliest Delft experimental investigation. In fact, the results of the model tests conducted by TU Delft may suffer from a high blockage effect due to the small cross-sectional area of the measuring section. As mentioned before in the experimental set-up of TUHH, a 2 mm gap between the root edge of the foil and the inner wall of the measuring section was needed to allow the force balance to measure the forces acting on the foil. As expected, this gap can lead to a considerable reduction of the lift coefficient.

In the numerical simulations, the dimensions of the foil and the cross section of the Delft cavitation tunnel were used; for this reason, the numerical results agree better with the Delft test results than with those of the other experimental investigations. The SST turbulence model, in particular, yields results that are fairly comparable to the Delft results in all CFD simulations.

Figure 7 shows the span-wise distribution of C_L. Note that the C_L distribution closely follows the contour of the leading edge. The intensity of the bound vortex correlates with the span-wise changes in the circulation, which in turn are reflected in the gradient of C_L. This relationship is shown on the right side of the figure, where a larger C_L variation indicates a stronger trailing edge vortical structures. This is further confirmed by the time averaged Q plot, especially at a value of 50 shown in the same figure.

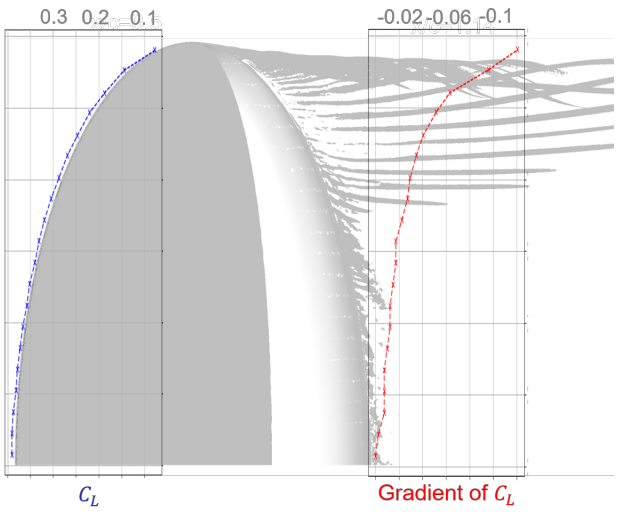

Figure 7: Features of C_L distribution in the span-wise direction, TUHH.

Vortex structures

The vortex structures are represented using the Q-criterion. Figure 8 shows instantaneous results from three different contributions: one from SCHOTTEL using the SST turbulence modeling approach, and two from CNRS and TUHH using DES approaches. All three contributions effectively capture the leading vortex and parts of the trailing vortex. However, the higher numerical diffusion in the results obtained by the SST model and the limited grid resolution of CNRS in the wake region result in a less defined trailing vortex downstream of the foil compared to the TUHH result. The TUHH simulation represents more details of the physical roll-up process initiated by the flow around the foil tip. This observed phenomenon is closely related to the lift distribution (see Figure 7).

Table 7: Main features of the numerical computations for the non-cavitating condition.

Institution	Code	Convection	Turb. model	$\Delta t \times 10^{-6}$ [s]
TUHH	ANSYS CFX	Bounded central difference	DES	2.2
SCHOTTEL	OpenFOAM	Unbounded second order upwind scheme	SST	50
CNRS	ISIS-CFD	Bounded central difference	SST DDES	150 37
MARIN	ReFRESCO	Second order upwind (QUICK) scheme	IDDES	193
SIREHNA	STAR-CCM+	Unbounded second order upwind scheme	SST	100

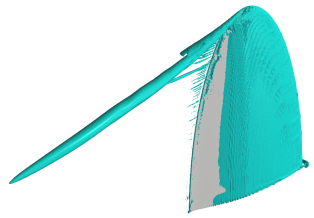

SST, SCHOTTEL.

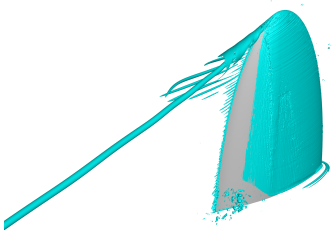

DDES, CNRS.

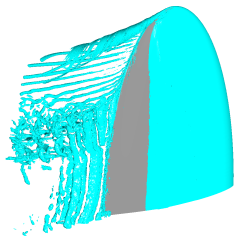

DES, TUHH.

Figure 8: Illustration of the instantaneous vortex structures by using Q-criterion with Q=50.

Flow Characteristics Along the Longitudinal Direction at the Tip Vortex Core

Trajectory of Tip Vortex Core Center

In most contributions, the center of the tip vortex core is determined by identifying the maximum Q values of the time-averaged flow field. However, at TUHH, Both EFD and CFD methods involve the use of wandering-corrected flow data. This correction is achieved by statistically analyzing the instantaneous centers based on the maximum Q values ($\max Q$). Additionally, the TUHH CFD approach includes the minimum pressure ($\min P$) and maximum Rotex/Liutex $\max R$ [19] [20] [30] as the alternative methods to identify the location of the tip vortex center. Notably, the results indicate a close alignment of wandering-corrected flow data determined by both $\max$Q and $\max R$ methods. In a later paragraph, it will be shown that various methods exhibit different representations of Reynolds stresses. In addition, SCHOTTEL illustrates the effect of mesh size on the sensitivity of the tip vortex core quantities. A coarser mesh (cMesh), compared to the finer mesh (fMesh) consisting of approximately 15 million cells.

In the analysis of the longitudinal trajectory, presented in Figure 9 and Figure 10, the vertical displacement of the vortex core center shows a slight difference between simulations and measurements. However, differences are observed in the horizontal direction. The experimental data shows a maximum displacement at about $x/c \approx 0.7$. Following that, a decline (TUHH) and a subsequent stabilization (CNR) might be noted. In contrast, the numerical results show a continuous increase in the y-displacement.

Table 8: Lift coefficient values under different test conditions for non-cavitating flow.

Institution	Facility/Numerical Model	Cross-section B × H [m × m]	v_∞ [m s^{-1}]	C_L
EFD				
TUHH	Wind tunnel	3 (Open side) × 2	16.4	0.544
CNR	Circulating water channel	3.6 × 2.25	3	0.480
Delft	Cavitation tunnel	0.3 × 0.3	6.8	0.651
CFD				
TUHH	DES	0.3 × 0.3	6.8	0.611
SCHOTTEL	SST	0.3 × 0.3	6.8	0.688
CNRS	SST	0.3 × 0.3	6.8	0.654
CNRS	DDES	0.3 × 0.3	6.8	0.670
MARIN	IDDES	0.3 × 0.3	7.15	0.647
SIREHNA	SST	0.3 × 0.3	6.8	0.672

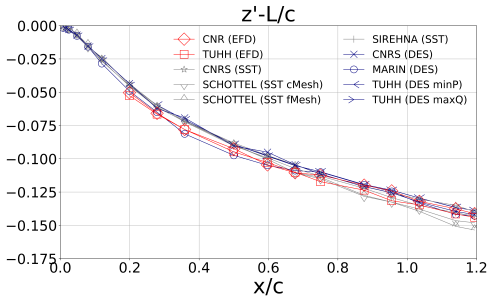

Figure 9: Vertical displacement of the tip vortex center.

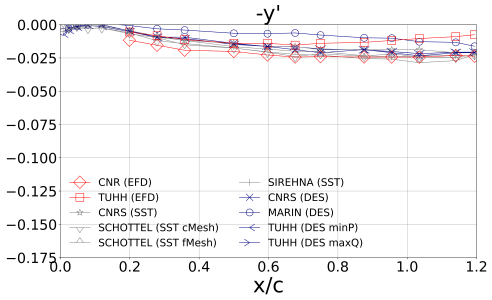

Figure 10: Horizontal displacement of the tip vortex center.

Max. Longitudinal Velocity and Minimum Pressure

The analysis in Figure 11 compares the longitudinal simulated and measured maximum values of the longitudinal velocity component within the tip vortex core. The calculated absolute maximum, which occurs just behind the trailing edge of the foil, is observed to be 1.5 to 2 times the inflow velocity. Note that the location of this maximum velocity is not necessarily at the center of the core, which is likely due to factors such as pressure gradients, flow separation at the trailing edge, and the influence of the leading edge vortex.

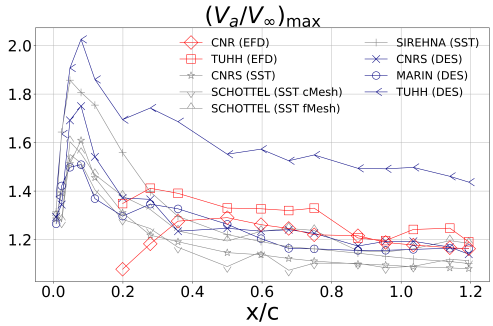

Figure 11: Comparison of the maximum value of the longitudinal velocity component in the core region.

As the distance from the foil increases, the maximum longitudinal velocity of the tip vortex decreases and eventually stabilizes at a level above the inflow velocity. This behavior, where the measured velocity exceeds the inflow velocity, is also observed in numerical simulations. In terms of pressure, Figure 12 shows a significant decrease within the core region. Overall, the results of the DES simulations show a larger pressure

drop than the results of the SST model, with the TUHH DES simulations showing the lowest pressure values. An exception is the SIREHNA SST result which has an absolute minimum pressure comparable to the TUHH DES result, but which are in agreement with other SST results further downstream. These observations enable a more detailed analysis of cavitating flow in a following paragraph.

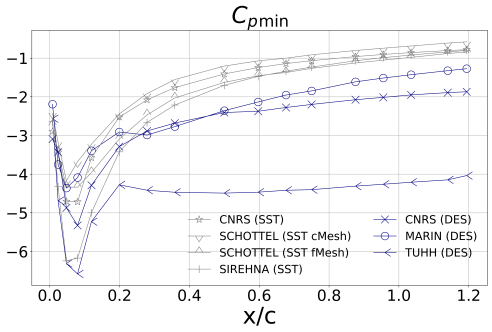

Figure 12: Comparison of the calculated minimum pressure in the core region.

Q at the Vortex Center

Figure 13 compares computed and measured maximum Q values at the vortex core center downstream the foil. It is important to notice that due to the nature of the stereoscopic measurements at CNR, the evaluation of the Q-criterion lacks the velocity gradients along the x-direction. However, the gradients along the x-direction are vastly smaller than the velocity gradients along the other two axes. Therefore, the influence of the velocity gradients along the x-direction on the Q-criterion value is very small and can be considered to be negligible.

TUHH's measured Q values remain nearly constant between $x/c = 0.2$ and 1.2. In contrast, CNR-Q values show a tendency of continuous decay, which might be attributed to a higher turbulence level in the experimental facility.

CFD-results indicate the highest Q values near the trailing edge, followed by a gradual decrease. TUHH's DES computations closely match TUHH's measurements. CNRS and MARIN, using DES techniques, exhibit a gradual decrease in maximum Q. Conversely, the RANS-SST results from CNRS, SIREHNA and SCHOTTEL are almost identical, although different mesh resolutions are used. Overall, it can be concluded that in the results of the RANS-SST simulations the value of Q in the initial area downstream of the foil is underpredicted and a clear decline along the x-axis can be observed.

Further results obtained by TUHH show that the value of Q at the point of minimum pressure is very close to the maximum Q within the vortex core. This comparison points out the uncertainties in identifying the vortex core center, especially due to the vortical flow interactions.

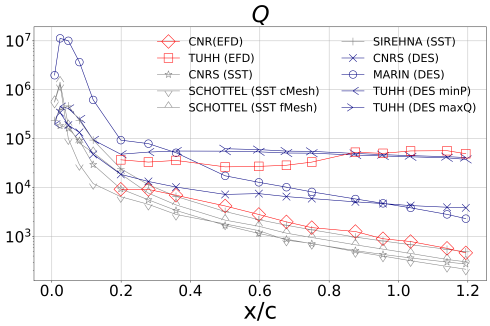

Figure 13: Comparison of the decay rate of the maximum Q-values at the core center.

TKE at the Vortex Center

Figure 14 shows the evolution of TKE values at the vortex center. CFD simulations show the highest turbulence levels shortly after the foil tip, likely due to the complex tip vortex formation process, with a notable decrease extending to approximately x/c=0.2. In the figure, TUHH results represents only the resolved part of the TKE, which accounts for more than 85% of the total TKE. Consequently, the TUHH TKE data starts at P7.

Experimental studies indicate higher TKE compared to CFD simulations, possibly due to a higher background TKE. The SST approach yields lower TKE than experimental measurements and most DES approaches. The differences between SST and DES simulations are attributable to their different modelling approaches.

Comparing the CNRS and TUHH ($\max Q$) DES results, both show similar TKE at the vortex center. However, the use of the $\min P$ method results in significantly lower TKE values, see TUHH $\min P$ results. This suggests that the tip vortex center TKE values are highly dependent on the vortex center identification method, in contrast to the Q-value observations which show minimal sensitivity to that.

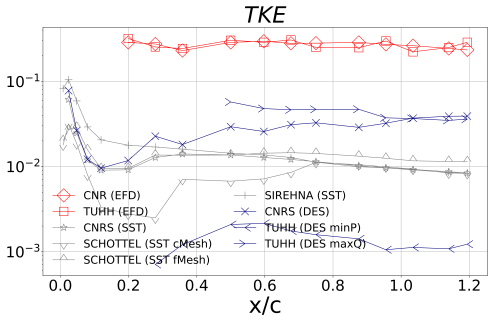

Figure 14: Longitudinal comparison of the TKE at the core center.

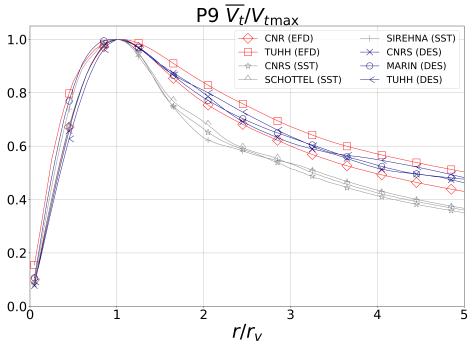

Figure 15: Radial profiles of the tangential velocity component.

Circumferential Averaged Quantities

Tangential Velocity Component

Capturing the characteristics of the vortex in the cross section is essential to accurately model the tip vortex flow. Figure 15 shows the tangential velocity component at the measurement plane P9, normalized by the individual maximum tangential velocity peaks. In general, within the viscous radius ($r/r_v \leq 1$), there is good agreement between the measured and simulated results. However, in the region far outside the viscous radius ($r/r_v > 1$), the DES results are within the range of the measured values, while the RANS-SST model tends to under-predict.

The discrepancy between TUHH's experimental and simulation results grows with increasing distance downstream of the foil, which may be due to the not well refined numerical grid. Moreover, the tangential velocity decay is more pronounced with higher free-flow turbulence [11], emphasizing its impact in the turbulent viscous flow region beyond the viscous vortex core.

In the context of the AVT-320 joint research project, the focus extends beyond station P9. The investigation includes of the corresponding values at different stations from P7 to P16. Both the EFD and the CFD results obtained by TUHH show a remarkable consistency: the tangential velocity peak remains mostly unchanged. This observation is consistent with the previous observations [5] [25] [27], and emphasizes the self-similarity characteristic of the maximum tangential velocity.

The rotation rate, $\omega = \overline{V_t}/r$, within the viscous core radius exhibit consistency across various contributions, appearing to be unaffected by differences in turbulence models and grid resolutions.

Longitudinal Velocity Component

High pressure gradient can result in the excess of axial velocity, while the presence of a wake vortex may reduce it. The longitudinal velocity profiles are influenced by the interaction between the tip vortex and the rolled-up vortex wake.

Figure 16 illustrates the variation of the longitudinal velocity component up to five times the viscous core radius at P9. Notably, its maximum value occurs near the viscous radius ($r/r_v = 1$) rather than at the vortex center ($r/r_v = 0$). The maximum values between $r/r_v = 0$ and $r/r_v = 1$ exhibit wide variation across different contributions, resulting in a considerable scatter of results in the viscous core region. This scatter is further influenced by the choice of turbulence models and grid resolution, which affect the accuracy of capturing the pressure.

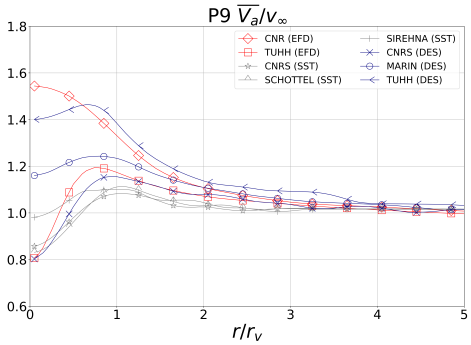

Figure 16: Radial profiles of the longitudinal velocity component.

Circulation

The data from Figure 17 show significant differences in the growth rate of the circulation inside and outside the viscous core. Inside the viscous core radius, viscous effects cause the tangential velocity to increase along

the radius, resulting in a faster growing circulation. In contrast, outside the viscous core radius, the tangential velocity decreases due to the predominance of potential-like flow, resulting in a slower circulation growth rate.

Experimental results from TUHH consistently show an increase in circulation of the tip vortex downstream of the foil, indicating an ongoing roll-up process. Modeling this effect in CFD simulations is challenging, mainly due to the high demand on the grid resolution required not only in the vortex core but also in the region surrounding the trailing edge vortices.

Note that the circulation here is non-dimensionalized by the maximum tangential velocity and the viscous core radius. The circulation (Γ) in the RANS-SST simulations can be underestimated due to the larger viscous core radius, while the results from DES approach range between the CNR and TUHH measurements.

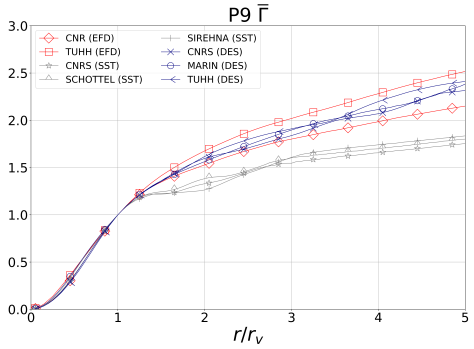

Figure 17: Radial profiles of the circulation.

Flow Characteristics of the Tip Vortex in a Selected Station

The EFD results shown in his part are without wandering correction, except for R_{yy}, as this correction clearly influences the properties of the distribution of this Reynolds tensor component.

Figure 18 compares the longitudinal velocity component at measurement station P9. Trailing edge wake effects are evident, with higher velocity on the suction side (tip vortex side) and lower velocity on the pressure side attributed to trailing edge vortices. The contours illustrate the roll-up process and emphasizes the high-velocity region in the tip vortex core. Most of the CFD simulations and TUHH experiments capture the low-velocity region near the vortex core and highlight the increased longitudinal velocity component in the vortex core region.

Figure 19 shows a comparison of the transverse velocity component, revealing minimal disparities among

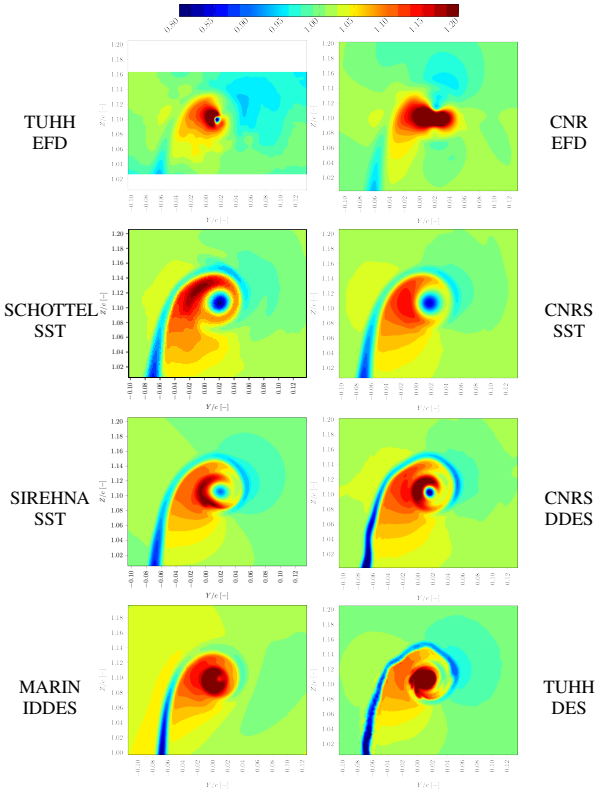

Figure 18: Longitudinal Velocity Component.

the numerical and experimental results. The general structure of the transverse velocity component is consistently reproduced by the methods applied.

In Figure 20, the vertical velocity component is presented, revealing a notable resemblance among the approaches, with minor discrepancies. The main distinction lies in the size of the isolated high-velocity region induced by the roll-up process. Otherwise, the vertical velocity component shows a consistent pattern across all the numerical and experimental results.

In Figure 21, the Q-criterion highlights the core of the tip vortex, depicting a region with a high positive Q-criterion where vorticity dominates. This vorticity-dominated area is encircled by another region with negative Q values, indicating areas dominated by strain rate. The results of the applied DES methods closely mimic to the experimental results, showing more intense and focused vortices. In contrast, the RANS approach results in vortices that are less compact and more dispersed. This comparison highlights the significant differences in the ability of RANS and DES to model vortical flows.

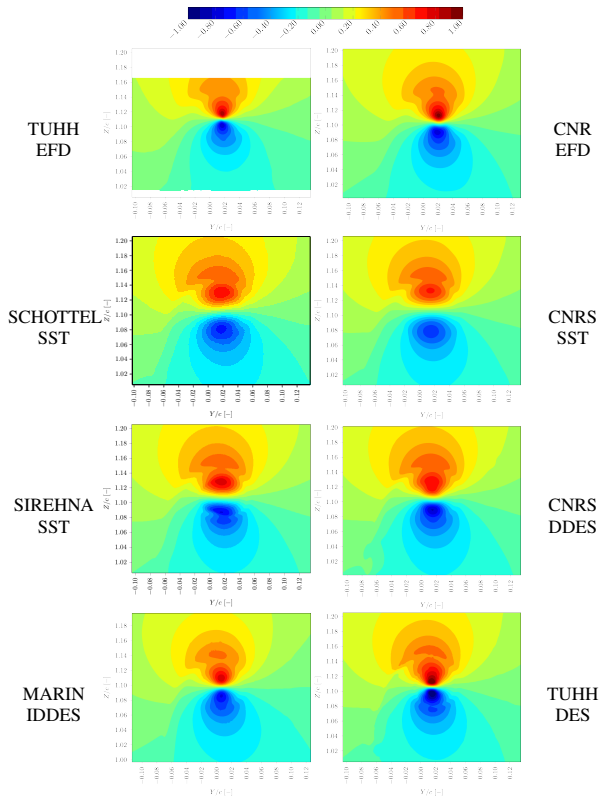

Figure 19: Transverse Velocity Component.

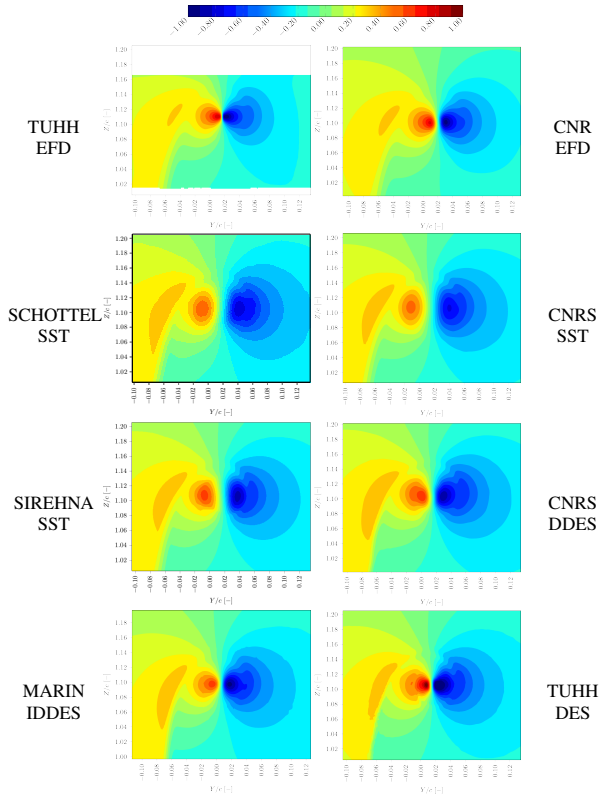

Figure 20: Vertical Velocity Component.

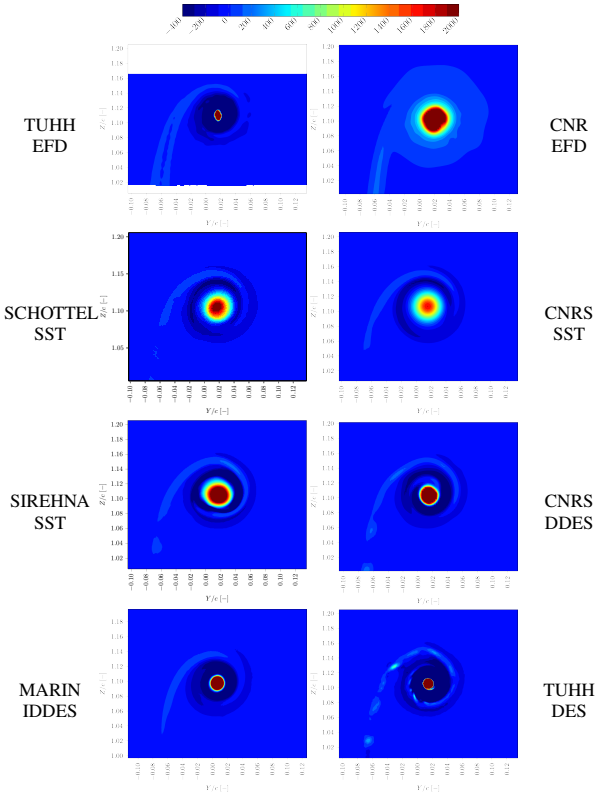

Figure 21: Q-Criterion.

Figure 22 illustrates the diagonal Reynolds stress tensor R_{xx} at measuring station P9. The experimental fluctuations in CNR results are markedly higher than the experimental fluctuations and the computational results, possibly due to the inherent limitations of stereoscopic approaches in accurately capturing out-of-plane quantities.

Concerning R_{yy} in Figure 23, it is noteworthy that the computational results of DES based methods show fluctuations align along the horizontal axis, while in the computational results of the RANS-SST simulations, fluctuations follow an inclined axis. Regarding the TUHH experimental results, this variable is corrected to reduce the effect of meandering of the vortex. This correction leads to a reduction in the fluctuations along the horizontal axis.

Regarding R_{zz} in Figure 24, the fluctuations in the experimental results are consistent with DES based methods results. In both TUHH experimental and CNRS numerical results, the fluctuations align along the vertical axis. However, in the results obtained by the RANS-SST methods, the fluctuations follow an inclined axis, seemingly perpendicular to the inclined axis of the R_{yy} fluctuations.

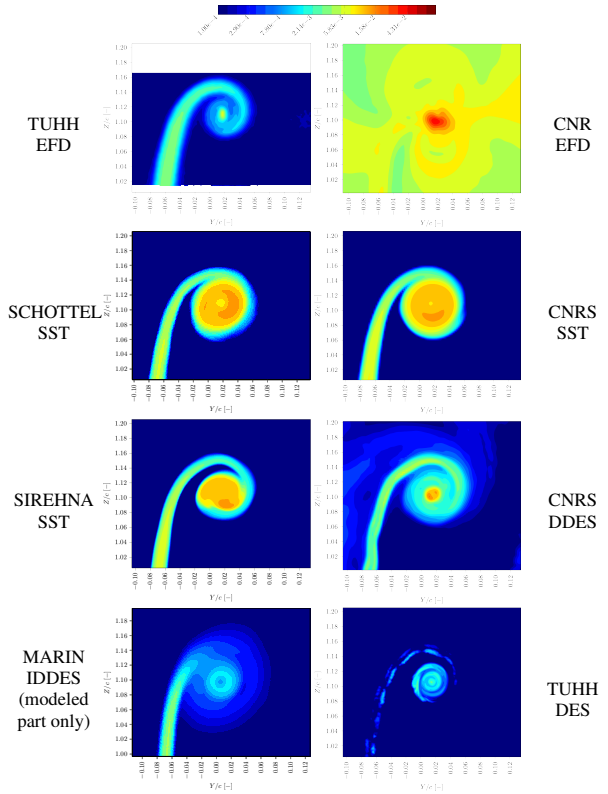

Figure 22: Reynolds Stress Tensor $\overline{u'_x u'_x}$

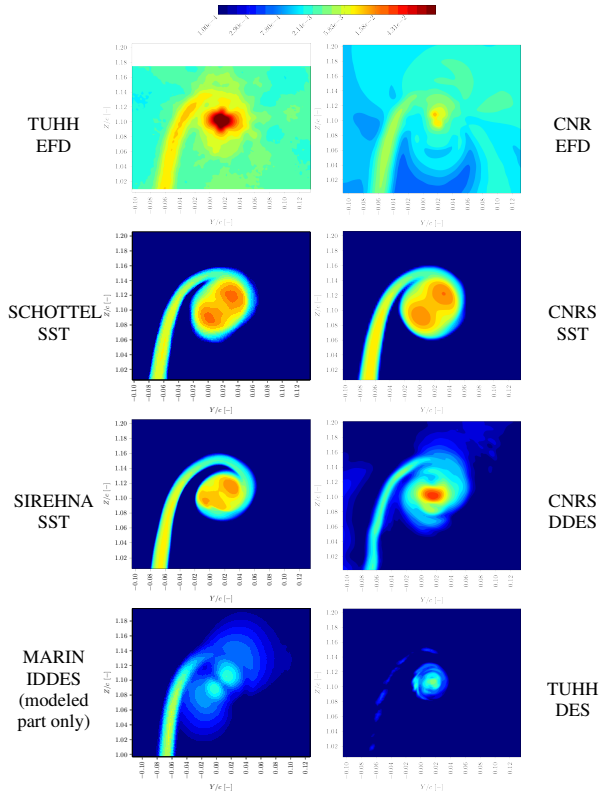

Figure 23: Reynolds Stress Tensor $\overline{u'_y u'_y}$

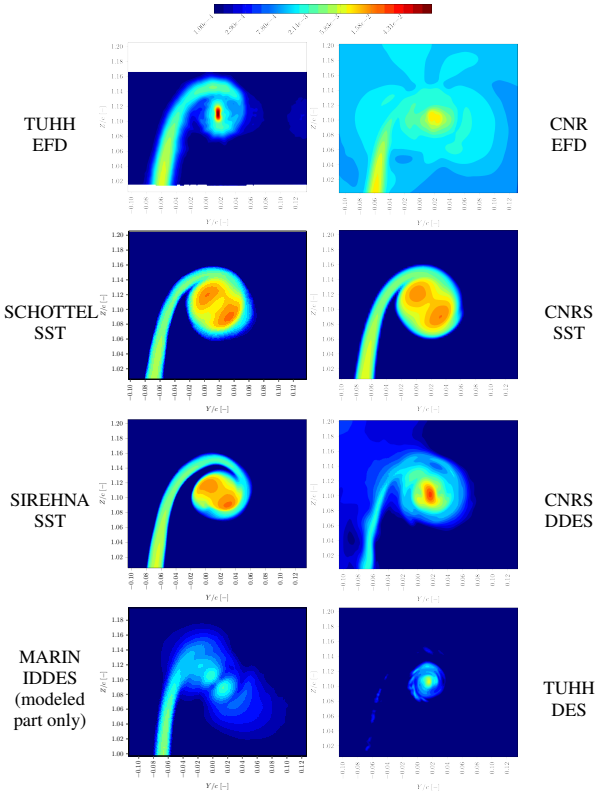

Figure 24: Reynolds Stress Tensor $\overline{u'_z u'_z}$

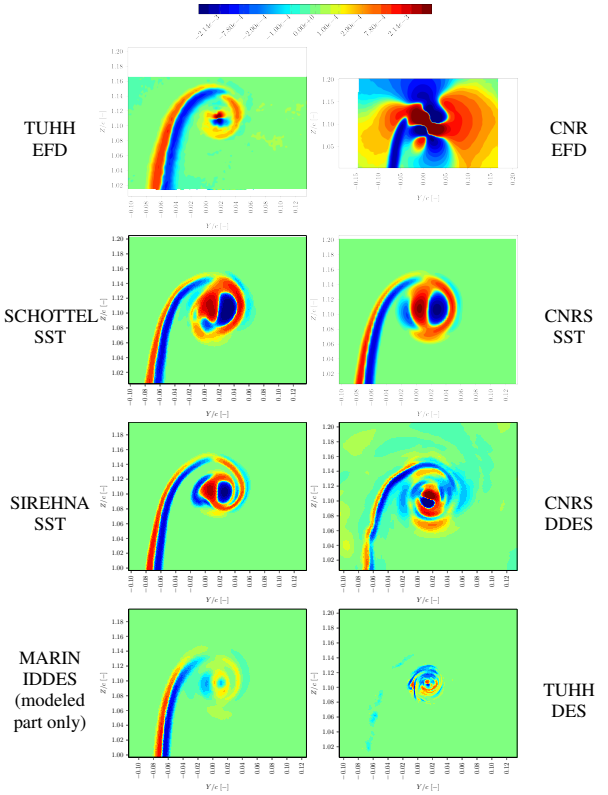

Figure 25: Reynolds Stress Tensor $\overline{u'_x u'_y}$

The experimental results obtained at TUHH, along with the DDES results from CNRS and DES results from TUHH, exhibit an almost good agreement for the Reynolds stress tensor R_{xy}, as depicted in Figure 25. Additionally, the results from SCHOTTEL SST, SIREHNA SST, and MARIN IDDES align well with the earlier findings in the roll-up region.

Similar to the R_{xy} results, there is a good agreement between the experimental results presented by TUHH, the DDES results from CNRS, and the DES results from TUHH for R_{xz} as depicted in Figure 26. The vortex core exhibits a structure that appears to be vertically oriented. In contrast, the vortex core structure in the remaining CFD results is horizontally oriented.

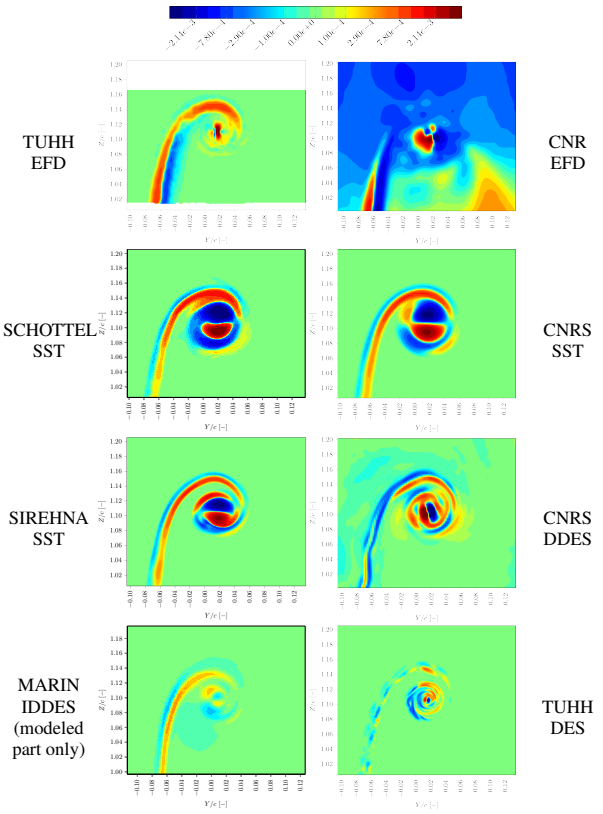

Figure 26: Reynolds Stress Tensor $\overline{u'_x u'_z}$

Figure 27 depicts the well-known four-leaf clover structure of the vortex core in the R_{yz} stress tensor. The structure is inclined at approximately $45°$ in the EFD results obtained by TUHH and CNR, which agrees with DDES results from CNRS, and DES presented by TUHH. In contrast, the remaining numerical computations display a vertically and horizontally aligned structure.

In Figure 28, the maximum TKE is observed in the core of the tip vortex, with notable differences in absolute values between experimental and numerical results. In the region of the trailing edge-induced vortices,

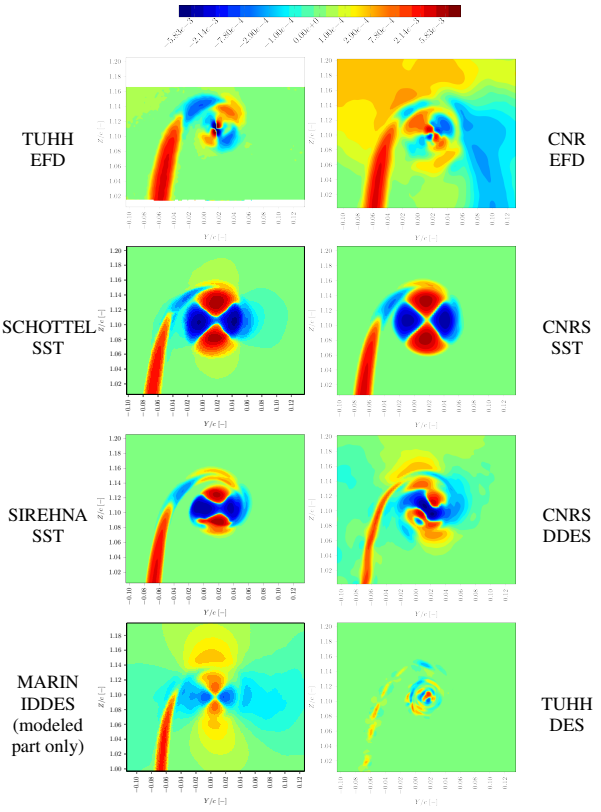

Figure 27: Reynolds Stress Tensor $\overline{u'_y u'_z}$

there is a substantial increase in TKE values. The analysis of the Reynolds stress tensor components reveals that the y-component and z-component contribute to TKE much more than x-component.

The good agreement between the MARIN IDDES results and the other DES results and experimental data is remarkable given the much coarser grid that has been used. However, as discussed in [18], this is considered to be related to a modeling (commutation) error as the turbulent kinetic energy of the wing boundary layer that is in the RANS region is not transferred to turbulent velocity fluctuations in the vortex region located in the LES region. Therefore, the resolved Reynolds stresses are negligible in the vortex region, and the modeled stresses are much smaller than typical RANS SST results.

Investigation of the Influence of Wandering Correction on the TUHH Numerical Simulation Results of Non-Cavitating Flow

The main purpose of the wandering correction is to reduce the uncertainty by the comparison of measured and calculated flow measurements near a tip vortex due to global fluctuation in the flow field. This correction allows a detailed study of the core characteristics of the vortex.

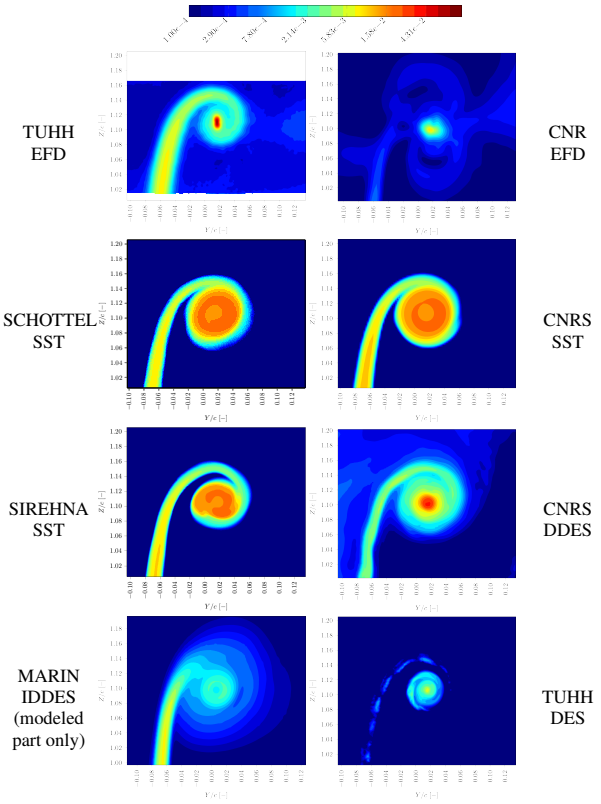

Figure 28: Turbulent Kinetic Energy

The contour plot shown previously at TUHH simulations were obtained without applying wandering corrections to the vortex center. During the wandering correction process, each instantaneous vortex center's position is adjusted according to the flow field, aligning it to a fixed point. The adjusted flow fields, such as velocities, are then averaged across all data samples to derive a corrected mean. To identify the location of each instantaneous vortex center, various methods can be employed. In this study, the vortex center locations are determined using $\min P$, $\max Q$, and $\max R$.

Figure 29 shows velocity fluctuations over a data set of 662 snapshots. This visualization is used to illustrate the correlation between v' and w', as shown in Figure 30 where a principal axis is highlighted with red arrows. The TKE including Reynolds stress contours are shown in Figure 31 and Figure 32.

Using $\min P$, the velocity fluctuations are significantly reduced, resulting in the lowest TKE intensity. In contrast, $\max Q$ and $\max R$ indicate that the fluctuations in v' and w' are uncorrelated, leading to a circular pattern in the TKE. According to the results of these methods, R_{yy} has a horizontal contour, while R_{zz} has a vertical contour. In particular, R_{yz} forms a pronounced clover-like pattern, but this is only clearly observed when corrections are performed using $\max Q$ and $\max R$. This corrected pattern aligns more closely with the experimental results than the uncorrected one.

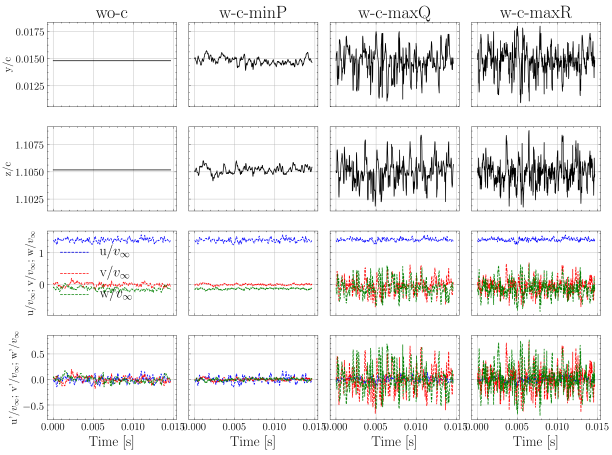

Figure 29: Tip vortex center fluctuations.

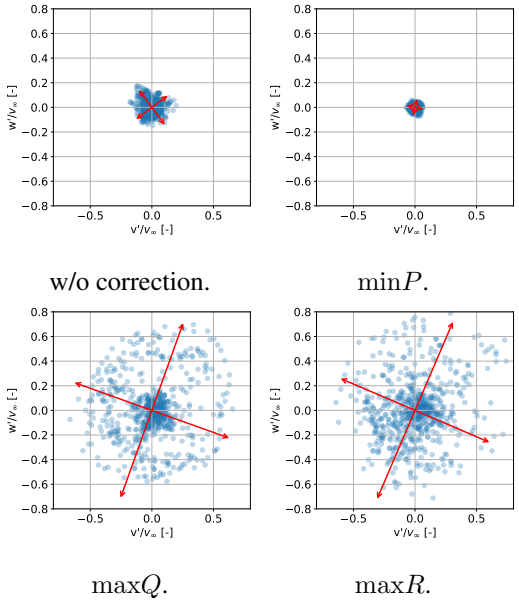

Figure 30: Correlation of v' and w' of the vortex core center in different identification methods.

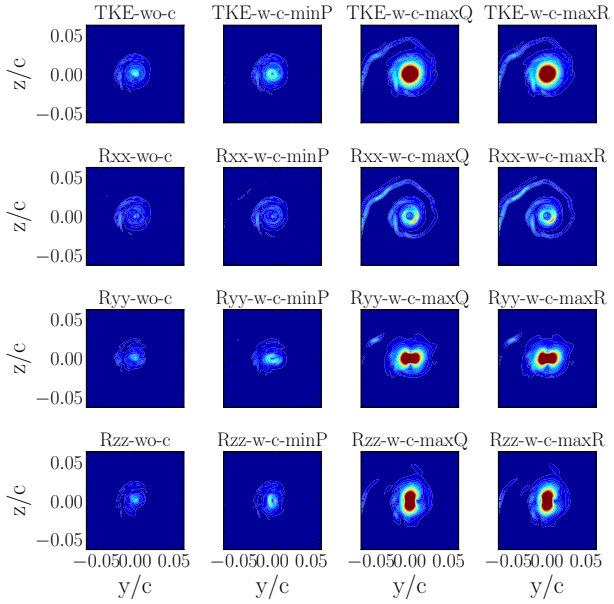

Figure 31: Normal stresses ([0, 0.01]).

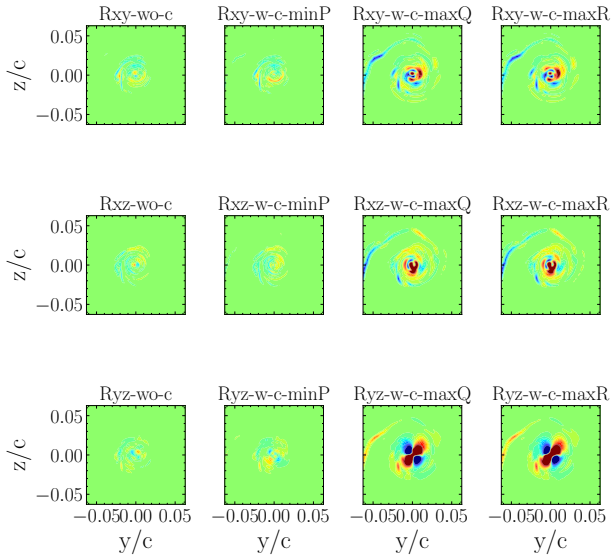

Figure 32: Shear stresses ([-0.0025, 0.0025]).

Flow Characteristics of the Tip Vortex under Cavitating Conditions

For the simulation of cavitation flows using an Eulerian mixture approach, the mass transfer between the liquid and vapour phases must be taken into account via a cavitation model. Most cavitation models use a formulation based on the Rayleigh-Plesset equation to calculate a special source term that is integrated into the continuity equation to model the formation and growth of a vapour bubble in a liquid. The Volume Of Fluid (VOF) method is applied to simulate the change of the Fluid properties as a function of the water vapour mixture in each control volume. Both phases, liquid and vapor, share the same velocity and pressure fields, treating the mixture as a homogeneous Eulerian fluid.

Both CNRS and TUHH use similar computational settings to simulate cavitation as for wetted flow simulations, corresponding to a cavitation number of 4.2. In contrast, SCHOTTEL performs cavitation simulations with extended cavitation numbers of 1.2 and 2.6. To model the cavitating condition, CNRS and SCHOTTEL use the SST turbulence model, while TUHH uses the hybrid RANS-LES (DES) approach. The results of the wetted flow simulations are used as initial conditions for the cavitating flow simulations. When the value of C_p falls below -4.2, it indicates that the pressure is below the saturation threshold and triggers the activation of the mass transfer model. In both RANS simulations, the area where C_p is less than -4.2 shows a high degree of similarity between the wetted and cavitating conditions, whereas the result of TUHH simulations reveals a distinct progression of the minimum C_p profiles along the tip vortex, as illustrated in Figure 33.

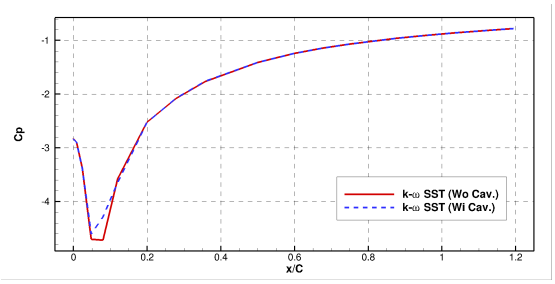

CNRS.

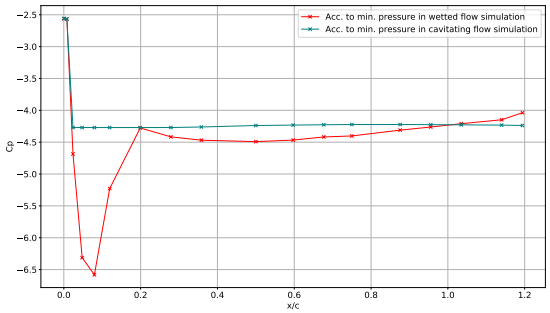

TUHH.

Figure 33: Evolution of C_p in the wetted and cavitating flow simulation conditions.

Figure 35 provides a comparative analysis, incorporating 727 snapshots from the cavitating flow simulation and 662 from the wetted flow simulation.

The core center in these simulations is identified using the minP method. To ensure a comprehensive analysis, the values shown in Figure 36 have been averaged across these snapshots. In a vortex, the tangential velocity initially increases with radial distance, peaks at the viscous core radius, and then gradually decreases. This pattern in cavitating flow can be divided into three distinct regions. In the first region, the cavitation core, velocity variations are significantly reduced compared with the non-cavitating case as the internal driving pressure approaches saturation pressure. The second region marks the transition from cavitating to wetted flow and is characterized by a sharp increase of the negative pressure that can speed up the flow. Finally, in the third region, beyond the cavitation interface, the flow returns to the typical wetted flow behavior. In the TUHH calculations, it is observed that the radius of the cavitating core is smaller than that of the non-cavitating viscous core. Near the cavitating core, the radial velocity components show more pronounced variations compared to the non-cavitating simulation. This pronounced variation could enhance the energy transfer between the vortex core and the surrounding external flow of the cavitating core. Consequently, this indicates that the cavitating vortex flow may be more persistent than the wetted vortex flow, especially in terms of maintaining the saturation pressure, as shown in Figure 34.

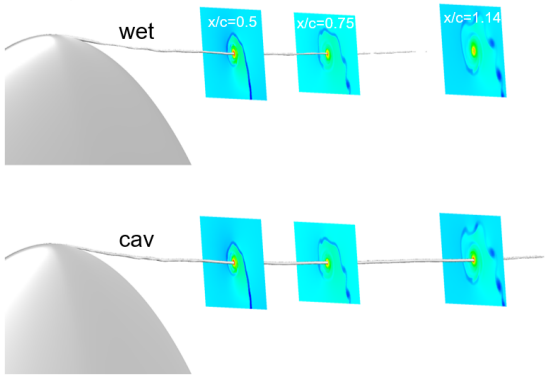

Figure 34: Isosurface of the saturation pressure and distribution of the longitudinal velocity component at three cross-sections, in both wetted and cavitating flow conditions, TUHH.

A reduction in the viscous radius at $\sigma = 4.2$ was also noted in previous CFD simulation [4]. However, as the cavitation number decreases, an increase in the viscous core is observed, aligning with findings from experimental research [23] and LES results [4]. This phenomenon may be related to the comparative sizes of the cavitating core radius and the viscous core radius.

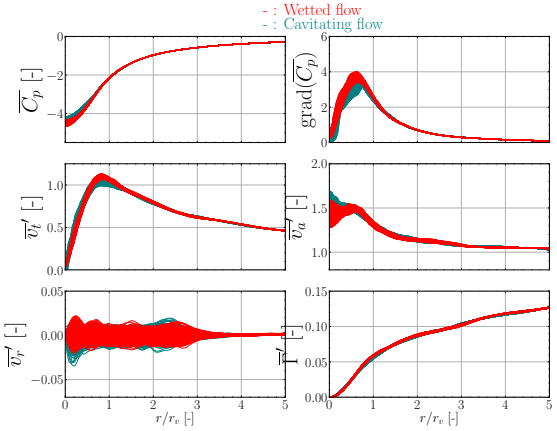

Figure 35: Snapshots of radially circumferential averaged quantities, TUHH.

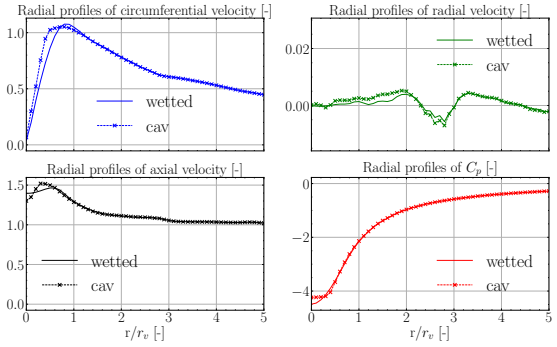

Figure 36: Mean radially circumferential averaged quantities, TUHH.

The results of SCHOTTEL SST simulations show that the cavity at $\sigma = 4.2$ is locally restricted to the immediate vicinity of the tip of the foil reaching $0.04c$ downstream, while $\sigma = 2.6$ and $\sigma = 1.2$ achieve a length of $0.33c$ and $1.13c$ respectively with the latter also experiencing a stable leading edge suction side cavitation extending about 10% of the foil. The vapor core radius is maintained at a constant $0.016c$ up to $0.75c$ downstream, after which it decreases with a reversed square root shape.

Due to the high axial and tangential velocities in the secondary vortex sheet, circumferential averaging of quantities can be misleading. However, some planes P7, P9, P11 and P16, as given in Figure 37, clearly experience a slight reduction of tangential velocities from the solid lines for the wetted cases to the dotted line for the cavitating cases with $\sigma = 1.2$. The maximum tangential velocity is slightly increased for the interrogation planes directly beyond the foil tip vapor cavity diameters, whereas later planes seem to be unaffected. This maximum is maintained at around two times the vapor core radius over the trajectory section

with a constant vapor core diameter. For outer radii the cavitating case tangential velocity distribution assumes the shape of the wetted case with minor positive offsets, leading to tangential velocities with a general slight increase. At the termination of the cavity at P16 the inner core and maximum velocity is increased, whereas the outer radii assume the identical velocity than the wetted case. Apparently the cavity termination leads to a boost of the kinetic energy in the vortex core.

The TKE is concentrated in the vapor phase with a rapid decrease just before reaching the interface radius. For the other cavitation numbers the cavity extent seems to be insufficient to alter the core flow significantly, except at the planes immediately downstream of the foil tip.

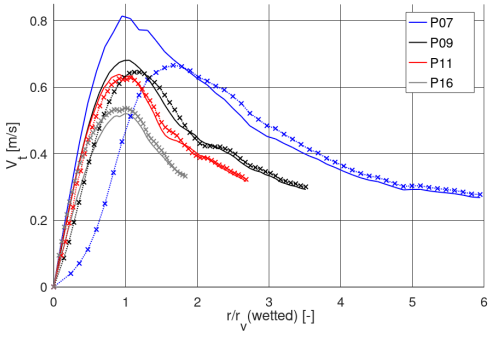

Figure 37: Circumferentially averaged tangential velocity in wetted and cavitating condition, r_v of wetted case, SCHOTTEL.

CONCLUSIONS & SUMMARY

The tip vortex properties of a specific elliptical foil was studied through various numerical analyses and experimental tests. Experimentally, two facilities were involved: the wind tunnel at Hamburg University of Technology (TUHH) and the circulating water channel at Consiglio Nazionale delle Ricerche (CNR). Numerically, five institutions (CNRS, MARIN, SCHOTTEL, SIREHNA, and TUHH) performed six simulations using different turbulence modeling techniques. The RANS - k-ω SST model was applied by CNRS, SCHOTTEL and SIREHNA. In addition, CNRS and MARIN performed simulations using Delayed Detached Eddy Simulation (DDES) and Improved Delayed Detached Eddy Simulation (IDDES), respectively, while TUHH used Stress-Blending Eddy Simulation (SBES). The objective was to evaluate the capability and limitations of these models in predicting turbulence details and pressure reduction within the vortex core. Significant differences were identified between the scale-resolved simulations and those using the eddy viscosity model.

The comparative analysis reveals that the RANS simulations presented here are inadequate in capturing essential quantitative aspects of tip vortices, such as concentrated vortex strength (Q criterion) and vortex core structures (Reynolds stresses). The RANS-based approaches are unable to capture the highly anisotropic nature of vortex structures in comparison to the more advanced hybrid SST-LES approach. Scale-resolved simulations are more consistent with experimental observations in representing turbulence structures, but discrepancies remain, particularly in DES simulations. These discrepancies are primarily due to differences in grid resolution and the balance between resolved and modeled turbulence, although the observations in the RANS simulations are quite similar. The comparative analysis reveals that the RANS simulations presented here are inadequate in capturing essential quantitative aspects of tip vortices, such as concentrated vortex strength (Q criterion) and vortex core structures (Reynolds stresses). The RANS-based approaches are unable to capture the highly anisotropic nature of vortex structures in comparison to the more advanced hybrid SST-LES approach. Scale-resolved simulations are more consistent with experimental observations in representing turbulence structures, but discrepancies remain, particularly in DES simulations. These discrepancies are primarily due to differences in grid resolution and the balance between resolved and modeled turbulence, although the observations in the RANS simulations are quite similar. The comparative analysis reveals that the RANS simulations presented here are inadequate in capturing essential quantitative aspects of tip vortices, such as concentrated vortex strength (Q criterion) and vortex core structures (Reynolds stresses). The RANS-based approaches are unable to capture the highly anisotropic nature of vortex structures in comparison to the more advanced hybrid SST-LES approach. Scale-resolved simulations are more consistent with experimental observations in representing turbulence structures, but discrepancies remain, particularly in DES simulations. These discrepancies are primarily due to differences in grid resolution and the balance between resolved and modeled turbulence, although the observations in the RANS simulations are quite similar. In addition, the TUHH wandering correction results show distinct differences between the $\min$P approach and the $\max$Q and $\max$R approaches. In particular, the Reynolds Stresses computed using the $\max$Q and $\max$R methods show remarkable similarities, resulting in a more clearly defined corrected flow field.

Accurate detection of tip vortex cavitation is challenging due to the difficulty in accurately determining pressure variations within the vortex. Not all DES-based methods effectively localize the rapid pressure gradients in the core region. These insights are crucial for understanding tip vortex behavior across different

conditions, both cavitating and non-cavitating conditions, and for predicting cavitation inception.

ACKNOWLEDGMENT

The work performed by the ECN/CNRS authors was granted access to the HPC resources made available by GENCI of IDRIS and CINES under allocations in recurrent annual projects no. 00129.

REFERENCES

[1] D. Acheson. Elementary Fluid Dynamics. Oxford University Press., 1990.

[2] R. Arndt, V. Arakeri, and H. Higuchi. Some observations of tip-vortex cavitation. Journal of Fluid Mechanics, 229:269–289, Aug. 1991.

[3] A. Asnaghi, U. Svennberg, and R. Bensow. Evaluation of curvature correction methods for tip vortex prediction in sst komega turbulence model framework. International Journal of Heat and Fluid Flow, 75:135–152, 02 2019.

[4] A. Asnaghi, U. Svennberg, and R. E. Bensow. Large eddy simulations of cavitating tip vortex flows. Ocean Engineering, 195:106703, 2020.

[5] S. C. C. Bailey, S. Tavoularis, and B. H. K. Lee. Effects of free-stream turbulence on wing-tip vortex formation and near field. Journal of Aircraft, 43(5):1282–1291, 2006.

[6] B. P. Chow J., Zilliac G. Mean and turbulence measurements in the near field of a wingtip vortex. AIAA Journal, 1997.

[7] W. J. Devenport, M. C. Rife, S. I. Liapis, and G. J. Follin. The structure and development of a wing-tip vortex. Journal of Fluid Mechanics, 312:67–106, 1996.

[8] P. A. Durbin. On the k-epsilon stagnation point anomaly. International Journal of Heat and Fluid Flow, 17:89–90, 1996.

[9] D.-F. Feder, M. Dhone, N. Kornev, and M. Abdel-Maksoud. Comparison of different approaches tracking a wing-tip vortex. Ocean engineering, 147:659–675, 2018.

[10] B. G. Axial flow in trailing line vortices. J. Fluid. Mech., 1964.

[11] H. C. Ghimire and S. C. C. Bailey. An experimental investigation of wing-tip vortex decay in turbulence. Physics of Fluids, 29(3):037108, 2017.

[12] E. Guilmineau, G. B. Deng, A. Leroyer, P. Queutey, M. Visonneau, and J. Wackers. Assessment of hybrid RANS-LES formulations for flow simulation around the Ahmed body. Computers & Fluids, 178:302–319, 2018.

[13] ITTC. Guideline on the uncertainty analysis for particle image velocimetry. In ITTC - Recommended Procedures and Guidelines, 2014.

[14] B. J. A mathematical model illustrating the theory of turbulence. Adv. Appl. Mech., 1948.

[15] C. Klaij and C. Vuik. Simple-type preconditioners for cell-centered, collocated finite volume discretization of incompressible reynolds-averaged navier-stokes equations. International Journal for Numerical Methods in Fluids, 71(7):830–849, 2013.

[16] M. Klapwijk, T. Lloyd, G. Vaz, and T. van Terwisga. On the use of synthetic inflow turbulence for scale-resolving simulations of wetted and cavitating flows. AIAA Journal, 57(3), 2021.

[17] A. Lidtke, T. Lloyd, F. Lafeber, and J. Bosschers. Predicting cavitating propeller noise in off-design condition using scale-resolving cfd simulations. Ocean Engineering, 254, 2022.

[18] R. Liebrand, M. Klapwijk, T. Lloyd, and G. Vaz. Transition and turbulence modeling for the prediction of cavitating tip vortices. Journal of Fluids Engineering, 143:011202, 2021.

[19] C. Liu, Y. Gao, S. Tian, and X. Dong. Rortex - a new vortex vector definition and vorticity tensor and vector decompositions. Physics of Fluids, 30(3):035103, 2018.

[20] C. Liu, Y.-s. Gao, X.-r. Dong, Y. Wang, J. Liu, Y. Zhang, X.-s. Cai, and N. Gui. Third generation of vortex identification methods: Omega and liutex/rortex based systems. Journal of Hydrodynamics, 31:1–19, 02 2019.

[21] S. Mozaffari, E. Guilmineau, M. Visonneau, and J. Wackers. Average-based mesh adaptation for hybrid RANS/LES simulation of complex flows. Computers and Fluids, 232:105202, 2022.

[22] C. Oseen. Über die wirbelbewegung in einer reibenden flüssigkeit. Ark. Mat. Astro. Fys, 7:035103, 1912.

[23] P. Pennings, J. Westerweel, and T. Terwisga. Flow field measurement around vortex cavitation. Experiments in Fluids, 56, Nov. 2015.

[24] F. Pereira, L. Eca, and G. Vaz. Simulation of wingtip vortex flows with Reynolds-Averaged Navier–Stokes and scale-resolving simulation methods. AIAA Journal, 57(3), 2019.

[25] W. Phillips. The turbulent trailing vortex during roll-up. Journal of Fluid Mechanics, 105:451 – 467, 04 1981.

[26] P. Queutey and M. Visonneau. An interface capturing method for free-surface hydrodynamic flows. Computers & Fluids, 36(9):1481–1510, 2007.

[27] B. R. Ramaprian and Y. Zheng. Measurements in rollup region of the tip vortex from a rectangular wing. AIAA Journal, 35(12):1837–1843, 1997.

[28] G. Rubino and M. Visonneau. Improved crossflow predictions for the one-equation γ transition model. Computers & Fluids, 245:105580, 2022.

[29] J. Wackers, G. Deng, E. Guilmineau, P. Leroyer, A. Queutey, and M. Visonneau. Combined refinement criteria for anisotropic grid refinement in free-surface flow simulation. Computers & Fluids, 92:209–222, 2014.

[30] Y. Wang, Y.-s. Gao, J. Liu, and C. Liu. Explicit formula for the liutex vector and physical meaning of vorticity based on the liutex-shear decomposition. Journal of Hydrodynamics, 31:464–474, 06 2019.

DISCUSSION

The authors are very grateful to the discussants (Philippe Spalart, Martin Renilson, Mattias Liefvendahl, and Peter Manovski) for their insightful comments, which which contributed to a detailed analysis of the results and increased the scientific value of the paper.

PHILIPPE SPALART, MARCH 10TH, 2024

This is the report on a large and excellent AVT programme, with discriminating comparisons between two experiments and six simulations. Both the measurement and simulation techniques are modern, and I think this would not have been possible even ten years ago. The birth of the trailing vortex sheet and tip vortex is of value under water, but also towards the performance and noise of airliners, wind turbines, and rotorcraft of all sizes.

I apologize for providing a long list of "areas for improvement." I am known for this. Please take it as a sign of interest, and a proof that this work has plenty of potential. Figures such as 18 and its followers are extremely instructive. Having redundancy for both sources is excellent.

1. Most importantly, the conclusion that "RANS simulations are inadequate" is questionable, when the SST-RC and SARC models have not been tried. These rotation corrections have a considerable effect on the vortex cores and the peak vorticity, Q, and jet velocity, which has been known since the work of Dacles-Mariani in the 1990's. I have great hopes for the turbulence-resolving methods, especially with the improving quality of grids, but still. The first task for industrial work may be to introduce rotation-corrected RANS models.

   Reply: The Spalart-Allmaras with Rotation/Curvature Correction (SA-RC) and the Shear Stress Transport with Curvature Correction (SST-CC) models still rely on the assumption of linear eddy viscosity. In the AVT-320 project, the Reynolds stress and mean strain rate components are evaluated. The plots show that there is no significant correlation between them. Furthermore, according to Abolfazl Asnaghi's research paper titled "Evaluation of curvature correction methods for tip vortex prediction in SST $k-\omega$ turbulence model framework" [3], it has been found that the curvature correction (CC) methods do not provide significant improvements in vortex prediction. This is because the effect on turbulent viscosity is either incorrect or insufficient. Further more, the models require additional empirical constants that must be adjusted for different flow regimes, which limits the generality of the models.

2. The rest of the comments are not given in order of importance. I wish the experimental design provided clear knowledge about turbulence in the boundary layer. The chord Reynolds number is under 10^6, so that thorough CFD simulations need the information. I presume they all assumed fully turbulent boundary layers. NACA662-145 is even an airfoil with laminar tendencies. The CNR tests might have a low lift because of laminar separation. XFOIL studies would be highly justified.
Reply: Obviously, more experimental results on the turbulence in the boundary layer would be very desirable in order to clearly understand the flow conditions in the near-wall region, which play an important role in the formation and development of the tip vortex. Unfortunately, due to the flow measurement techniques used, it was not possible to measure the boundary layer flow. It is planned to acquire this information in subsequent experiments. The domain dimensions and Reynolds number utilized in the CFD simulations are consistent with those used in the Delft experimental investigation. The results of the CFD simulations demonstrate a high degree of correlation with the Delft experimental result.
The significant differences in the lift coefficient are due to the different test conditions, such as the ratio of the model size to the dimensions of the measurement section. To investigate this aspect, additional RANS simulations were carried out using the same boundary conditions that were also used in the wind tunnel test at the TUHH. The calculated C_L was 0.581 without a gap and 0.544 with a 2 mm gap. Due to the limited cross-section in the cavitation channel at TU Delft, the lower pressure on the suction side of the foil can be clearly observed, as shown in Figure 38. From this observation, it can be concluded that the significant difference in the lift coefficient between the EFD results of the wind tunnel at TUHH and those of the cavitation channel at TU Delft is due in particular to the blocking effect and the different experimental setup, such as the height of the gap between the foil root and the bottom of the measuring section.

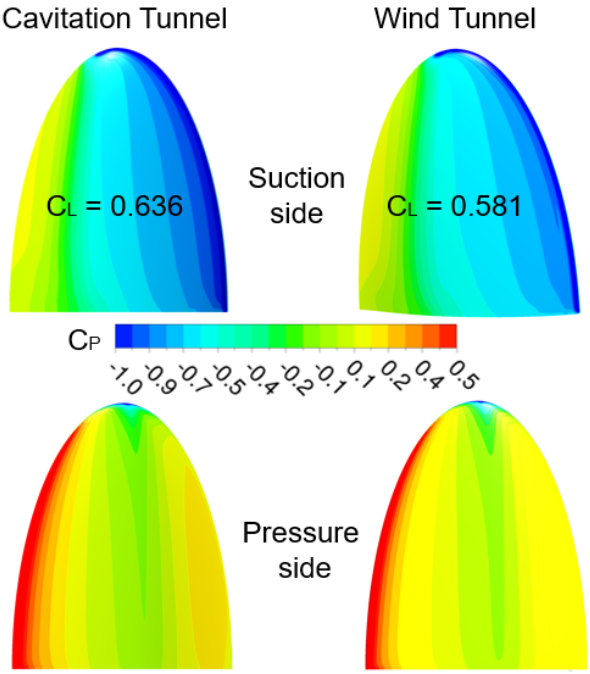

Figure 38: Pressure on the foil in the numerical cavitation tunnel and wind tunnel RANS simulations.

3. Figure 7 indicates that the sectional lift coefficient is proportional to the local chord. This is exactly what lifting-line theory would predict for an elliptical wing (although only at high aspect ratio). An elliptical loading gives uniform downwash in LLT, so that if the wing is untwisted, the local lift coefficient is constant. Pressure contours would confirm this, if the minimum is found to be independent of y.
Reply: Figure 39 shows the distribution of C_p on the suction side of the foil at different spanwise stations. The minimum value of C_p is observed in the vicinity of the leading edge of the foil. The position of the minimum C_p exhibits slight variation, ranging from 0.39% to 0.46% of the individual chord length; see Figure 40. The figure (right) shows that the minimum value of C_p increases as the tip region is approached.

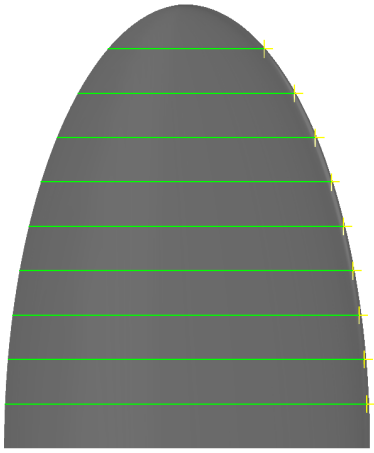

Nine polylines to capture the pressure distribution.

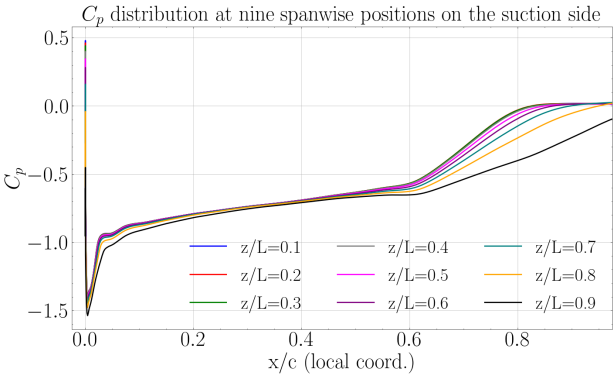

C_p distribution.

Figure 39: C_p distribution on the polylines at different spanwise positions.

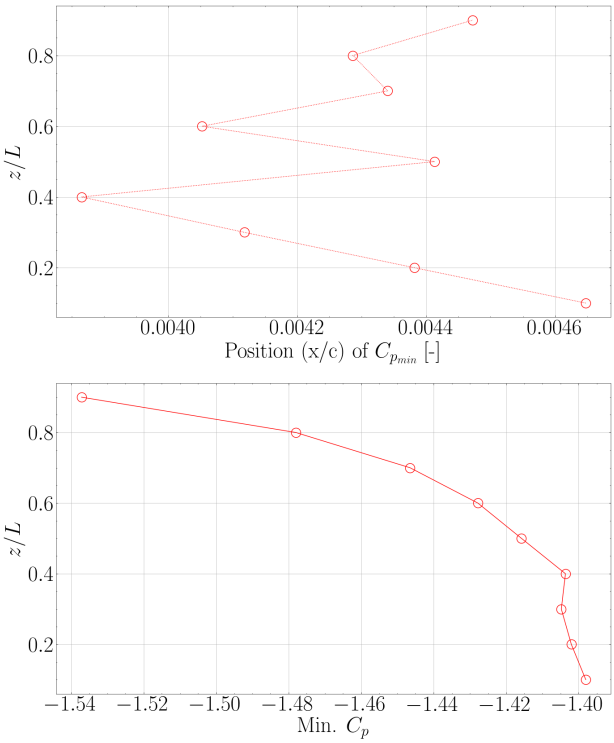

Figure 40: Positions and the values of minimum C_p at different spanwise positions.

4. Interpreting Fig. 8 is interesting. Recall that Q was crested to exhibit vortices, as opposed to shear layers. So, if a solution has a smooth vortex sheet coming off the trailing edge, it will carry no Q, whereas if it undergoes the Kelvin-Helmholtz instability, Q will appear. In other words, the three fields are not as different as the Q fields make it look.
Reply: The vortical structures associated with Q at the same level (Q=50) as Figure 8 in the paper is shown in Figure 41. The color on the foil represents the strength of the wall shear stress, from the high values (red) to the low values (blue). The separated flows originate at the start of the blue region, where the wall shear stress approaches zero.
Based on the observation from TUHH simulation, the Kelvin-Helmholtz instability is caused by the shear layer created at the point of separation. This instability creates vortices that are captured in the Q-structure as regions of high vorticity coming off the trailing edge.

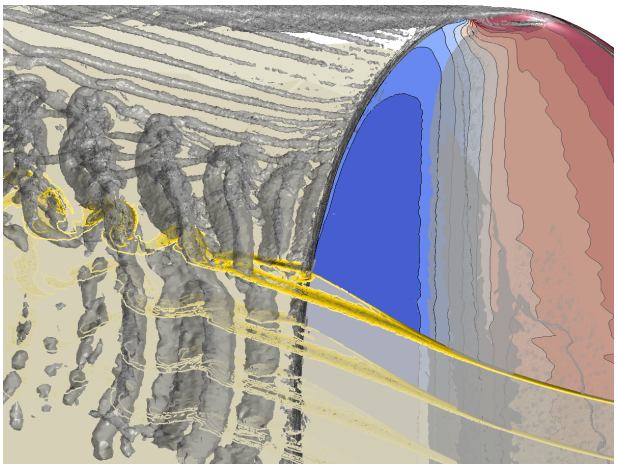

Figure 41: Trailing vortex from the separated flow.

5. The discussion of Fig. 13 omits the huge differences. Two orders of magnitude between the experiments! This is in strong conflict with Fig. 11.
   Reply: Figure 11 shows the highest axial velocity, which is not directly associated with Q. Figure 21 illustrates the Q plot, revealing that the CNR tip vortex region is more extensive in comparison to TUHHs. The difference of two orders of magnitude in Q at the center between the experiments is not entirely explained.

6. Figure 15 would be much more revealing if the quantities were not normalized using r_v and V_{tmax}. I'd love to "see" the circulation and core size. I predict the circulation would agree rather well in the inviscid region, as indicated in Figs. 19 and 20, so that we would identify differences due to turbulence closer to the axis. I doubt the conclusion that "SST under-estimates the circulation." If the lift is correct, the circulation cannot be far off.
   Reply: The radius of the viscous core in the RANS simulation is much larger than in the experiments and the DES simulation, see Figure 42. It is the reason why the dimensionless value of circulation in the RANS simulation is smaller beyond the viscous core region, if the circulation looks similar, as you mentioned.
   Figure 43 compares circulation, which has been made non-dimensionalized by chord length and inflow velocity. Within the EFD and DES viscous core regions, RANS simulations provide lower values for circulation. However, beyond the RANS viscous region (r/c≈0.025), the RANS circulation is found to be larger than that of the other results.
   The circulation may exhibit uniformity beyond the region under consideration because the plotted area is not entirely free from viscosity. Nevertheless, the analysis was confined to the region of the tip vortex core.

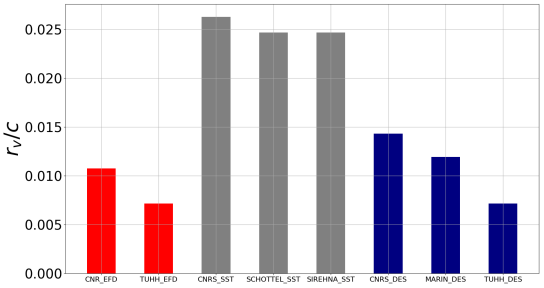

Figure 42: Viscous radius normalized by c.

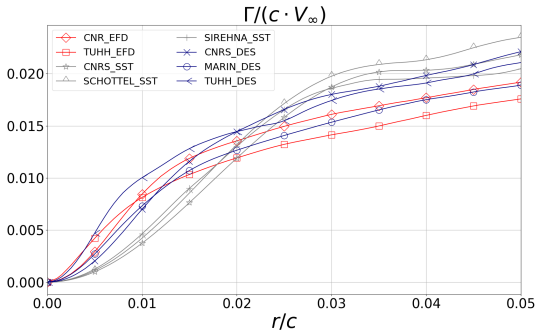

Figure 43: Circulation normalized by c and v_∞.

MARTIN RENILSON, 19 APRIL 2024

This paper describes the preliminary results of a very comprehensive and interesting piece of work with many international collaborators, and I would like to congratulate the authors on a well written paper. I certainly look forward to further published material from this project.

1. I also note quite a large difference in the experimental values of Q in figure 13. The authors say that discrepancies exist in the absolute levels of the computed values, and that the CNR-Q values deviate due to missing gradients in the x-direction in measurements. Am I right in assuming that this refers to the computed values from the experimental measurements, rather than the computations referred to in the next paragraph? If so, how big do the authors think that the difference would make to the experimentally quoted results in figure 13 if the information in the x-axis was not missing, and would that explain the difference between the two EFD sets of results?

Reply: A clarification has been added to the paper based on the analysis of the results from the TUHH experiments showing that the velocity gradients in the x-direction do not dominate the Q-value.The discussion of figure 13 in the paper has been adapted accordingly.

2. Were all the numerical calculations done "blind" without the organisations knowing in advance what the experimental results were?
   No, all numerical simulations were done after the Delft experiments.

3. I note that the authors conclude that the RANS simulations are inadequate compared to the hybrid SST-LES approach. I think that this is an important conclusion from this work. However, is it a fair "like-for-like" comparison? By this I mean that the computational effort involved with the hybrid SST-LES is a lot larger than RANS. If the grid size with the RANS was increased to result in the same level of computational cost as the hybrid SST-LES approach (perhaps with an adaptive mesh procedure) would that improve the RANS sufficiently to be "as good"?
   Reply: CNRS performed RANS and DES simulations at the same grid resolution, resulting in different visual representations, as shown in the comparative plots reported in the paper.
   The fine SCHOTTEL mesh can be considered a LES ready mesh in terms of resolution in the tip vortex region. However, the results from the fine mesh tend to be more consistent with the results from the course mesh in the RANS simulations.

4. How many grid points across the vortex core have been used for each of these numerical computations? I note that in earlier work by one of the authors (reference 3 in this paper), it is suggested that 32 grid points are required across the vortex core. What is recommended by the current authors?
   Reply: If the red region in the Q plot (Figure 21) is used to represent the size of the vortex core (where vorticity is dominant), the vortex core size in DES appears to be smaller compared to the size in RANS. It varies depending on the specific turbulence models used.
   Moreover, the Taylor microscale can be used as guidance for mesh refinement, but it is not sufficient for representing the dissipation range, which is, however, characterized by the Kolmogorov scale. The Taylor microscale is considerably larger than the Kolmogorov scale.
   An alternative approach is to utilize the turbulence ratio, which describes the relationship between the resolved and modeled parts of turbulence in LES simulations. This can be used to justify the grid resolution. In the TUHH simulation, the resolved part exceeds 90% in the vortex center. Nevertheless, the grid revolution must be continuously reduced until it reaches the Kolmogorov scale to resolve the smallest scale in turbulent flows.
   In addition, the foil geometry and boundary conditions of the flow can influence the resolved scales. In this context, for this specific case, we provide the grid spacing size instead of grid points, as listed in Table 6.

MATTIAS LIEFVENDAHL, APRIL 22TH, 2024

This study provides a wealth of detailed information about the structure of a tip vortex, based on both flow measurements and simulations. This is particularly important for the prediction of tip vortex cavitation. It also provides fundamental challenges for turbulence modelling, e.g. concerning the meaning of resolved and subgrid scales for an unsteady vortex with a turbulent core.

1. If the authors could provide some additional information concerning the initial state (at the tip) of the vortex, that would be quite interesting. Which parts of the foil boundary layer affects the vortex formation and is that boundary layer laminar? Furthermore, how is this initial state predicted in the simulations?
   Reply: The formation of the tip vortex is primarily due to the pressure difference surrounding the tip of the foil, which causes a swirling motion in the flow. Figure 44 illustrates the wall shear stress on the foil and the high strength of the vortical flow on the cross-planes of the tip vortex. From P0 to P3, the tip vortex is not yet established. The wall shear stress exhibits a decreasing trend downstream from the tip to the trailing edge on both the pressure side and the suction side. This observation suggests that the formation of the tip vortex may have an impact on the flow behavior in the boundary layer. A correlation exists between the boundary layer flow and the tip vortical flow. In all simulations, the flow was modelled as fully turbulent and the surface of the foil as a smooth wall. Further studies are required to investigate the behaviour of tip vortex formation in conjunction with the transition model in detail.

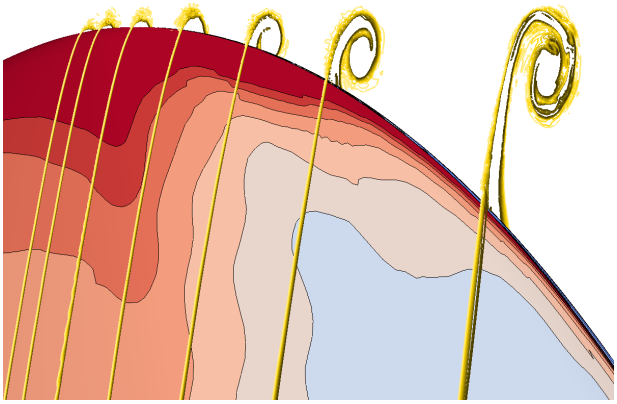

Wall shear stress on pressure side.

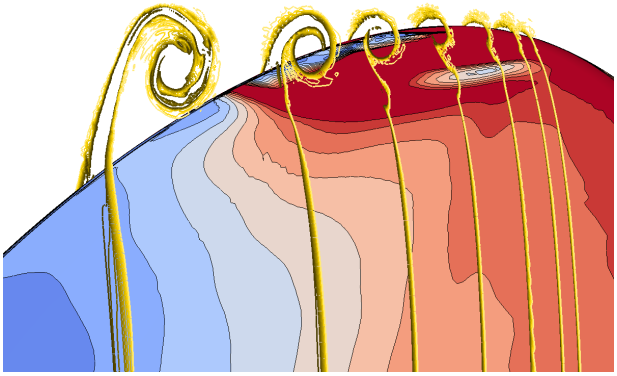

Wall shear stress on suction side.

Figure 44: Formation of the tip vortex.

2. In figure 14, measured TKE starts at, $x/c = 0.2$, with a relatively high level. Is that constituted by vortex oscillations or vortex core turbulence? On the same topic, what conclusions can be drawn from the simulation results of figure 14.
   Reply: The background turbulence is higher in the experiments than in the numerical simulations, which can influence the turbulence level in the vortex core region. In the DES simulation, the turbulence in the vortex core is partially resolved; the TKE value must be higher than the fully modeled TKE value in the RANS simulation. RANS models typically have a lack of sensitivity to the presence of the tip vortex, which can produce higher values of turbulent viscosity within the vortex core region.

3. The paper concludes that RANS computations are inadequate in capturing essential quantitative aspects of the tip vortex. This is a plausible conclusion, and it would be valuable if the authors could further highlight which results most strongly support it. For instance, judging by figure 28, which shows the TKE distribution through the vortex, there is a relatively large scatter of the results, also within each class of methods (EFD, RANS and scale-resolving simulations).
   Reply: The TKE in the RANS simulations has a similar pattern, while the pattern in the DES simulations is different. A relatively large scatter in the results is expected for two reasons: The first reason is grid resolution. The resolution directly affects the ability to resolve various scales of turbulence. A higher resolution allows for the capture of smaller turbulent eddies, providing a more detailed and accurate representation of turbulent flows. The second reason is related to the wandering correction. Figure 31 shows the corrected TKE after identifying the vortex core center in the TUHH simulation using different methods. They show different results as well.
   In general, the DES results are in better agreement with the TUHH EFD results than the RANS results.

PETER MANOVSKI, JULY 12TH, 2024

1. Suggestion: We have published a paper a while ago on different vortex core identification methods. We use POD and Gamma 1 criteria and find they are both very robust. You may find this analysis useful. http://dx.doi.org/10.1016/j.ijheatfluidflow.2020.108556.
   Reply: Thanks for your suggestions. The combined method of POD and Gamma 1 is very attractive. We will try it later in our experimental investigations. The results shown here for vortex center identification are based on the numerical simulations. We are not sure about the application of the POD analysis to filter out the less energetic flow, because in the tip vortex core small-scale turbulent eddies are responsible for the dissipation. It is important for the overall vortex dynamics and decay process. In addition, the Gamma 1-based method is primarily used for 2D analysis and may have limitations in fully 3D turbulent flows.